



**HAL**  
open science

## **WINDII, the Wind Imaging Interferometer on the Upper Atmosphere Research Satellite**

Gordon G. Shepherd, Gérard Thuillier, W. A. Gault, B. H. Solheim, C. Hersom, J. M. Alunni, Jean-Francis Brun, S. Brune, P. Charlot, L. L. Cogger,  
et al.

► **To cite this version:**

Gordon G. Shepherd, Gérard Thuillier, W. A. Gault, B. H. Solheim, C. Hersom, et al.. WINDII, the Wind Imaging Interferometer on the Upper Atmosphere Research Satellite. *Journal of Geophysical Research: Atmospheres*, 1993, 98 (D6), pp.10725-10750. 10.1029/93JD00227 . hal-01628657

**HAL Id: hal-01628657**

**<https://hal.science/hal-01628657v1>**

Submitted on 3 Feb 2021

**HAL** is a multi-disciplinary open access archive for the deposit and dissemination of scientific research documents, whether they are published or not. The documents may come from teaching and research institutions in France or abroad, or from public or private research centers.

L'archive ouverte pluridisciplinaire **HAL**, est destinée au dépôt et à la diffusion de documents scientifiques de niveau recherche, publiés ou non, émanant des établissements d'enseignement et de recherche français ou étrangers, des laboratoires publics ou privés.

# WINDII, the Wind Imaging Interferometer on the Upper Atmosphere Research Satellite

G. G. SHEPHERD,<sup>1</sup> G. THUILLIER,<sup>2</sup> W. A. GAULT,<sup>1</sup> B. H. SOLHEIM,<sup>1</sup> C. HERSOM,<sup>1</sup> J. M. ALUNNI,<sup>3</sup>  
 J.-F. BRUN,<sup>2</sup> S. BRUNE,<sup>4</sup> P. CHARLOT,<sup>5</sup> L. L. COGGER,<sup>6</sup> D.-L. DESAULNIERS,<sup>7</sup> W. F. J. EVANS,<sup>8</sup>  
 R. L. GATTINGER,<sup>9</sup> F. GIROD,<sup>5</sup> D. HARVIE,<sup>4</sup> R. H. HUM,<sup>10</sup> D. J. W. KENDALL,<sup>10</sup> E. J. LLEWELLYN,<sup>11</sup>  
 R. P. LOWE,<sup>12</sup> J. OHRT,<sup>4</sup> F. PASTERNAK,<sup>13</sup> O. PEILLET,<sup>14</sup> I. POWELL,<sup>9</sup> Y. ROCHON,<sup>1</sup>  
 W. E. WARD,<sup>1</sup> R. H. WIENS,<sup>1</sup> J. WIMPERIS<sup>15</sup>

The WIND imaging interferometer (WINDII) was launched on the Upper Atmosphere Research Satellite (UARS) on September 12, 1991. This joint project, sponsored by the Canadian Space Agency and the French Centre National d'Etudes Spatiales, in collaboration with NASA, has the responsibility of measuring the global wind pattern at the top of the altitude range covered by UARS. WINDII measures wind, temperature, and emission rate over the altitude range 80 to 300 km by using the visible region airglow emission from these altitudes as a target and employing optical Doppler interferometry to measure the small wavelength shifts of the narrow atomic and molecular airglow emission lines induced by the bulk velocity of the atmosphere carrying the emitting species. The instrument used is an all-glass field-widened achromatically and thermally compensated phase-stepping Michelson interferometer, along with a bare CCD detector that images the airglow limb through the interferometer. A sequence of phase-stepped images is processed to derive the wind velocity for two orthogonal view directions, yielding the vector horizontal wind. The process of data analysis, including the inversion of apparent quantities to vertical profiles, is described.

## 1. INTRODUCTION

### 1.1. Basic Instrument Concept

The WIND imaging interferometer (WINDII) takes advantage of airglow emission lines photochemically produced from species in the upper mesosphere (OH), the lower thermosphere (O<sub>2</sub>, O(<sup>1</sup>S)), and the middle thermosphere (O(<sup>1</sup>S), O(<sup>1</sup>D), and O(<sup>2</sup>P)) for the measurement of winds and temperatures in the altitude range 80 to 300 km. In this section we describe how an imaging field-widened Michelson interferometer is employed for this purpose.

When the optical path difference (the travel time delay between the two paths multiplied by the vacuum velocity of light) in a Michelson interferometer is scanned from zero to some final value, the resulting output is the Fourier transform (FT) of the spectrum, which can be expressed as follows:

$$S(\Delta) = \int_{-\infty}^{\infty} B(\sigma) e^{i2\pi\sigma\Delta} d\sigma \quad (1)$$

where  $\sigma$  is wavenumber and  $\Delta$  is optical path difference (OPD). In Figure 1a the Doppler-broadened (Gaussian) 557.735-nm atomic oxygen line,  $B(\sigma)$  (one of the emissions selected for WINDII), is shown for a temperature of 200 K. The computed FT,  $S(\Delta)$ , of this spectrum is shown in Figure 1b; it is a cosinusoid having a frequency corresponding to the center frequency of the line, modulated by the FT of the Gaussian line shape, which is another Gaussian, as shown. (The frequency here has been adjusted so that one cycle in the figure represents 20,000 actual cycles.) To obtain such an "interferogram" by direct measurement would require collecting about 1 million data points, requiring a very complex instrument that would not be practical for our application. However, a very simple configuration is capable of producing the information required. If the path difference is set to some reasonably large value and then is scanned over only one period of the cosinusoid (for which the optical term is one fringe), the Doppler velocity is manifested as a phase shift of this fringe. The modulation depth, which Michelson defined as fringe "visibility," namely, the ratio of amplitude to mean value, is directly related to the temperature. In this simple configuration the interferometer is a solid unit of cemented glasses, that includes a mirror cemented on piezoelectric drivers, so that it can be stepped in small steps over an OPD range of one wavelength.

If we let  $v$  be the wind velocity,  $k$  the interference order,  $c$  the velocity of light, then the phase shift is

$$\phi = 2\pi k \frac{v}{c} \quad (2)$$

For  $k \sim 10^5$  and  $v \sim 10 \text{ m s}^{-1}$ ,  $\phi = 1.2^\circ$ . This resolution is achievable by an instrument having a size compatible with space flight requirements.

<sup>1</sup>Institute for Space and Terrestrial Sciences, York University, Toronto, Ontario, Canada.

<sup>2</sup>Service D'Aéronomie du Centre National de la Recherche Scientifique, Verrières-le-Buisson, France.

<sup>3</sup>Quantel, Les Ulis Orsay, France.

<sup>4</sup>AIT Corporation, Ottawa.

<sup>5</sup>CNES Centre Spatial de Toulouse, Toulouse, France.

<sup>6</sup>University of Calgary, Calgary, Canada.

<sup>7</sup>CAL Corporation, Ottawa.

<sup>8</sup>Trent University, Peterborough, Ontario, Canada.

<sup>9</sup>National Research Council of Canada, Ottawa.

<sup>10</sup>Space Science Division, Canadian Space Agency, Ottawa.

<sup>11</sup>University of Saskatchewan, Saskatoon, Canada.

<sup>12</sup>University of Western Ontario, London, Canada.

<sup>13</sup>MATRA-ESPACE, Toulouse, France.

<sup>14</sup>BERTIN, Aix les Milles, France.

<sup>15</sup>Interoptics, Ottawa.

Copyright 1993 by the American Geophysical Union.

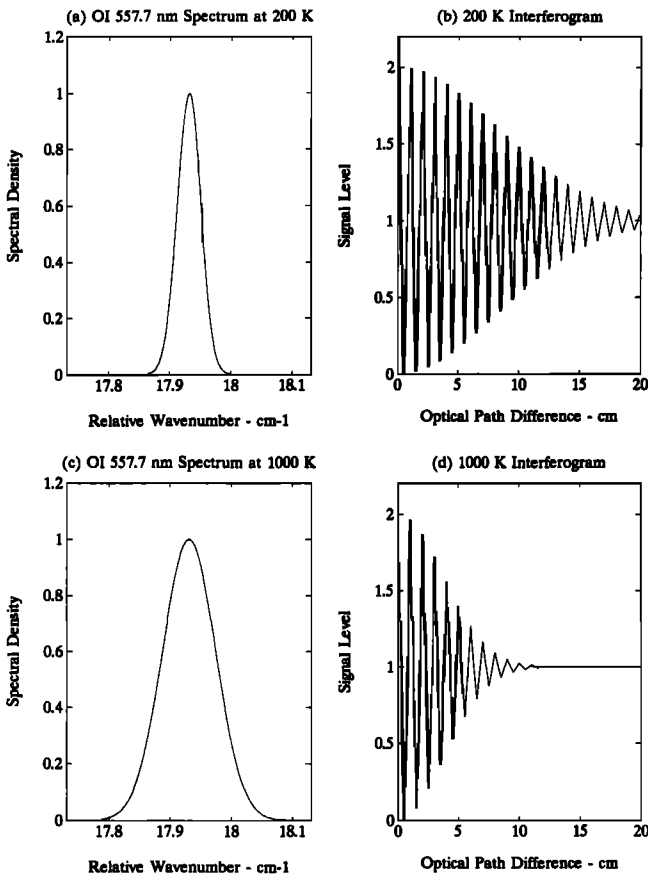


Fig. 1. (a) The spectral line shape of the atomic oxygen 557.7-nm emission at 200 K and (b) the corresponding Fourier output of a Michelson interferometer (MI) called an interferogram. (c) The 557.7-nm spectral line shape for 1000 K and (d) the corresponding interferogram. For the interferograms, one cycle in the figure represents 20,000 actual cycles.

For the determination of the temperature the fringe visibility  $V$  is related to the temperature  $T$  by

$$V = \exp[-Q_0 \Delta^2 T] \quad (3)$$

$V$  is the line visibility as given by (3) where  $Q_0 = 1.82 \times 10^6 / (M \lambda_0^2)$ ,  $M$  is the atomic mass (gram) of the species emitting the line centered at  $\lambda_0$ , and  $\lambda_0$  is the line wavelength at rest.

In Figure 1c we show the line shape for the same atomic oxygen 557.735-nm emission shown in 1a but for a temperature of 1000 K. The effect on the interferogram is shown in Figure 1d, which illustrates through comparison with Figure 1b that the temperature can be determined at a fixed path difference, by stepping the OPD over a single fringe.

The equation corresponding to the interferograms of Figure 1 but defined in terms of an instrument that makes small OPD steps of size  $x$  from a reference optical path difference  $\Delta_0$  is, where we have changed our variable from  $\sigma = 1/\lambda$  to  $\lambda$ ,

$$S(x) = I_0 \left[ 1 + UV \cos 2\pi \frac{\Delta_0 + x}{\lambda} \right] + I_B \quad (4)$$

$I_0$  is the line intensity;  $\lambda$  is the Doppler-shifted line wavelength ( $\mu\text{m}$ );  $U$  is the visibility reduction factor introduced

by the instrument; and  $I_B$  is the atmospheric background light which enters the interferometer through the interference filter selecting the atmospheric line to be observed.

Since only three parameters (visibility, phase, and mean intensity) can be extracted from an interferogram,  $I_B$  needs to be measured by another means, following which it is subtracted from  $S(x)$  to form the background-corrected signal  $I(x)$ :

$$I(x) = S(x) - I_B \quad (5)$$

The requirement of determining the absolute phase ( $2\pi\Delta/\lambda$ ) is avoided by using a relative phase  $\phi = 2\pi\Delta/\lambda - 2\pi m$ , where  $m$  is an unknown integer and  $\phi < 2\pi$ . The penalty for this is that the "zero-wind" phase must be determined later through instrument calibration.

After generating an interferogram by varying  $x$  from 0 to  $\delta$ , we may calculate

$$J_1 = \frac{1}{\delta} \int_{i=0}^{\delta} I(x_i) dx \quad (6)$$

$$J_2 = \frac{2}{\delta} \int_{i=0}^{\delta} I(x_i) \cos \frac{2\pi x_i}{\lambda} dx \quad (7)$$

$$J_3 = -\frac{2}{\delta} \int_{i=0}^{\delta} I(x_i) \sin \frac{2\pi x_i}{\lambda} dx \quad (8)$$

When the summation is made over an integral number of fringes, we have

$$J_1 = I_0 \quad (9)$$

$$J_2 = UVI_0 \cos \phi \quad (10)$$

$$J_3 = UVI_0 \sin \phi \quad (11)$$

from which  $I_0$ ,  $V$ , and  $\phi$  may be determined if  $U$  is known.

The actual procedure used for WINDII atmospheric data is described in section 3.1. Knowledge of  $V$  leads to the temperature as already described, and  $\phi$  is the total phase which includes the intrinsic interferometer phase ( $\phi_i = 2\pi m$ ), the phase induced by the velocity of the spacecraft ( $\phi_s$ ), the phase induced by the Earth rotation ( $\phi_r$ ), and the phase induced by the wind to be measured ( $\phi_w$ );  $\phi_i$ ,  $\phi_r$ , and  $\phi_s$  depend on the line of sight position in the instrument field of view and are known either from calibration data or calculated from the spacecraft attitude and velocity. Having  $\phi$  from above and knowing  $\phi_i$ ,  $\phi_r$ , and  $\phi_s$ , one can then derive  $\phi_w$  from the measured  $\phi$ . The wind velocity along the particular line of sight used for the measurement is calculated from

$$\phi_w = \frac{2\pi}{\lambda_0} D \frac{v}{c} \quad (12)$$

where  $D$  is the interferometer effective optical path difference given by [Thuillier and Hersé, 1991].

$$D = \Delta - \lambda_0 \frac{\delta \Delta}{\delta \lambda} \quad (13)$$

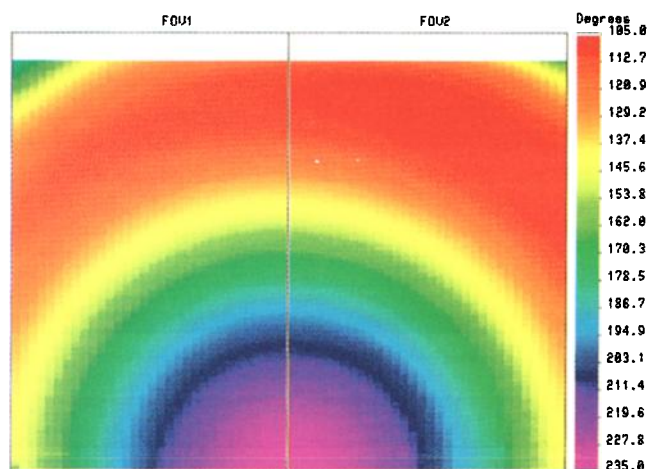


Plate 1. WIND imaging interferometer (WINDII) phase image for 738.4 nm obtained from the Argon on-board calibration lamp. Note the color scale which extends from 105° to 235°. The image is symmetrical about the bottom center of the CCD image, which is the location of the Michelson interferometer axis. Because of field widening, the phase variation is only 130°, over an off-axis angular change of 10° inside the interferometer.

Its value is measured during the instrument characterization and is available for use.

An example of a phase image for the 738.4-nm line from the on-board Argon spectral lamp (Table 4) is shown in Plate 1, as obtained from a sequence of four images, applying (6)–(11) on a pixel by pixel basis. The phase begins at 235° on the interferometer optical axis located at the center bottom of the CCD and falls to about 100° at the top, before rising to 160° at the corners. This small variation in phase is observed because the Michelson interferometer is field-widened, otherwise the phase change would be several hundred thousand degrees.

Array detectors, such as CCDs, provide a capability for quantitative imaging using just a camera lens and a CCD. In principle, a camera can be made into a spectroscopic imager by placing a band-limiting element in front of the camera lens. However, all spectral band-limiting elements introduce a transmittance that is dependent on the off-axis angle. Interference filters such as employed in WINDII have a wavelength of peak transmittance given by  $\lambda_i = \lambda_p i^2 / 2n^2$ , where  $\lambda_p$  is the wavelength of peak transmittance for normal incidence,  $\lambda_i$  is the wavelength of peak transmittance at angle  $i$ , where  $i$  is the incident angle of the ray and  $n$  is the effective refractive index of the interference filter. The transmittance of the band-limiting element thus varies across the image in a way that depends on the quantities introduced above and the passband width. The Fabry-Perot etalon presents a more extreme case in which spectral rings are superimposed on the image. Such devices still qualify as imagers, such as the Rees *et al.* [1984] Doppler imaging interferometer and the Kendall *et al.* [1985] Oglow camera, but the spatial information is mixed with the spectral information, the two being multiplied together. Of course one cannot record two-dimensional spatial information and spectral information on a single two-dimensional detector; a choice must be made.

With WINDII the intent is to record full two-dimensional spatial images characterized by a single OPD value; an

internal mirror movement is used to step the OPD value through four (or eight) positions and record an image at each position. We have chosen to make the OPD steps sequential in time in order to achieve full imaging in the sense that a wind value is obtained for every pixel for which sufficient airglow emission exists to make a measurement. In fact, the OPD does vary over the field of view, producing the type of phase variation in the image shown in Plate 1, but because the interferometer is field-widened, the variation is small enough to be readily calibrated. An interference filter is also required in front of the Michelson to select particular emission lines. The instrument transmittance for a single emission does vary over the field of view, but again it is a variation that can be readily calibrated. This characteristic can also be exploited: one of the WINDII filters is adjusted so that it transmits OH emission at the bottom of the image (the lowest altitude) and O<sup>+</sup> emission at the top. For the O<sub>2</sub> emission, which has closely spaced rotational lines, different lines are imaged at different places on the CCD.

The measured velocity we have described thus far is simply the component along the line of sight. WINDII employs two view directions, at 45° and 138° from the velocity vector on the anti-Sun side of the spacecraft. Images taken simultaneously in both directions are recorded side by side on a single CCD. Pairs taken roughly 7 min apart are combined to give orthogonal wind vectors from the same volume of atmosphere, on the assumption that the wind does not change in that time.

## 1.2. Heritage

In response to the Upper Atmosphere Research Satellite (UARS) mission opportunity announced in 1978 the wind and temperature by remote sensing (WINTERS) instrument proposed by France with G. Thuillier as principal investigator was one of those selected in 1979. It was based on the concept of a field-widened Michelson interferometer [Bouchareine and Connes, 1963] which uses refractive materials in the arms of the interferometer to provide much larger fringes, at a given path difference, than for an ordinary Michelson interferometer. Hilliard and Shepherd [1966a, b] conceived a simple configuration of this instrument, operating at an essentially fixed path difference, for the measurement of atmospheric temperature. This instrument had great sensitivity for temperature but could not be used for wind measurements due to its inherent sensitivity to instrument temperature change. A passive system designed to cancel this undesirable effect was proposed by Thuillier and Shepherd [1985] and adopted by the WINTERS instrument and its ground-based version called MICADO. The approach is an extension of the method described by Title and Ramsey [1980]. The WINTERS instrument based on the Thuillier and Shepherd [1985] concept includes optical fibers, photomultiplier detectors, and mechanical scanning of the two fields of view as in the high-resolution Doppler imager (HRDI) design. The UARS mission was not approved for implementation until 1984, and by that time there were insufficient resources available in France to build the entire instrument. It was therefore agreed to join forces with Canada, in order to share the cost but also to take advantage of what had already been developed in both countries. Canada had developed, for a Spacelab flight, an instrument called wide angle Michelson Doppler imaging interferometer (WAMDII)

[*Shepherd et al.*, 1985], which took advantage of recently developed CCD technology as well as new piezoelectrically driven positioners. In France, studies had been carried out for the WINTERS project and construction had begun on the MICADO instrument which was to be operated as a correlative measurement experiment during the UARS flight.

The combination of fundamental concepts available from the WINTERS and WAMDII thus formed the basis of a new instrument, called WINDII. The remainder of this paper is concerned with a presentation of the WINDII instrument.

### 1.3. *Expected Contribution to Upper Atmosphere Research Satellite (UARS) Goals*

The UARS mission is dedicated to the measurement of energy input, abundances of minor species, temperature, and winds in the stratosphere and mesosphere in order to study their mutual relationships and to build and validate atmospheric models. The wind is a key to the understanding of atmospheric behavior because it transports energy and species from one location to another and represents the response of the atmosphere to the net forcing imposed on it. The importance of wind measurement was acknowledged early in the history of the study of the Earth's atmosphere, but actual data for the stratosphere, mesosphere, and lower thermosphere have been slow to appear, owing to the intrinsic difficulty of the measurement. For this reason, indirect means involving the assumption that the winds satisfy some sort of balance condition have typically been used for their determination. The wind field most simply calculated and most often presented is that based on geostrophic balance and the observed temperature fields [*Andrews et al.*, 1987, pp. 224–225] although other alternatives have been explored (see *Randel* [1987] or *Marks* [1989] for a discussion). This indirect method, however, only addresses the large-scale average winds and suffers significant difficulties at low latitudes, where the geostrophic balance breaks down, and at high latitudes in the thermosphere where electromagnetic forces start playing a significant role in driving the neutral circulation [*Richmond*, 1991]. In addition, the assumption that the circulation is constantly in balance has never been directly verified on a global basis and the nature of this balance is one of the topics we hope to address with WINDII. Another region of particular interest to WINDII is the extratropical upper mesosphere/lower thermosphere where one of the dominant sources of energy is the dissipation of gravity waves and tides. The nature of the dynamics in this region has traditionally been examined using the transformed Eulerian mean equations, the temperature fields, and the radiative transfer codes (see, for example, *Solomon et al.* [1986] or *Shine* [1989]). With a suitably averaged data set of horizontal winds from WINDII, it should be possible to examine these dynamics from a new perspective.

To date, most of the measurements of middle atmospheric winds have been obtained through the use of radiosondes, rockets, and radars. Optical instruments have provided a good deal of information about winds in the thermosphere through measurements from space [*Killeen and Roble*, 1988] and from the ground (see, for example, *Burnside et al.* [1981]; *Hernandez et al.* [1982]; *Batten and Rees* [1990]; *Thuillier et al.* [1990]; *Wiens et al.* [1988]). This technique takes advantage of naturally occurring airglow emissions

above 80 km which contain information about wind and temperature. This information can be extracted by using interferometers such as those of Fabry-Perot or Michelson. The passive optical method is the most amenable to spaceflight.

WINDII is one of two UARS instruments dedicated to the measurement of atmospheric dynamics, specifically of global winds. The other instrument, HRDI, has as its primary goal the measurement of winds in the upper troposphere, stratosphere, and mesosphere using a triple-etalon Fabry-Perot spectrometer that observes the shifts of absorption lines in scattered sunlight. WINDII is a Michelson interferometer that measures the wavelength shift of emission lines in the Earth's airglow, beginning at 80 km near the mesopause and extending up through the thermosphere, with the primary emphasis being in the range 80 to 110 km. The design of HRDI revolves around the requirement of a single narrow passband, to permit the measurement of an absorption line in the presence of the large scattered white light background. This requirement leads to a small field of view. While it can also measure emission lines in the airglow, the dominant requirement makes it less sensitive than it would otherwise be, and so it will be used for that purpose on a limited basis.

The Michelson interferometer and the Fabry-Perot spectrometer are complementary by their nature, as one works in spectral space and the other in OPD space. WINDII has a very low tolerance to white light but has extremely high sensitivity; it is designed specifically for the study of weak airglow emissions. Thus the complement of HRDI and WINDII are well suited for covering the range of altitudes of interest for dynamics measurements to support the UARS mission. The Fabry-Perot instrument is well accepted for the measurement of winds, as demonstrated with the FPI instrument on the Dynamics Explorer 2 spacecraft [*Killeen et al.*, 1984; *Hays et al.*, 1984]; long before that, it was used for the spaceborne global measurement of temperature [*Thuillier et al.*, 1980; *Blamont and Luton*, 1972]. The wide angle Michelson is a less mature instrument, although the device had been under development for some time in Canada [*Hilliard and Shepherd*, 1966a, b; *Shepherd et al.*, 1984, 1985, 1991; *Ward*, 1988] and in France where the MICADO instrument is now operational in the field [*Thuillier and Hersé*, 1991; *Thuillier et al.*, 1990]. The UARS mission will provide the first spaceflight opportunity for this technique. The capability of HRDI and WINDII to make measurements in an overlapping altitude range permits an important opportunity to compare the results and performance of these two rather different approaches.

In the UARS mission, WINDII has the responsibility of extending the wind measurements, made at lower altitudes by HRDI, up to 110 km. For this purpose we use Doppler shifts of narrow emission lines emitted by the visual airglow. This restriction can be met by the choice of three prominent emissions: atomic oxygen O<sup>1</sup>S at 557.7 nm, at night a thin layer near 97 km, the O<sub>2</sub> atm band emission at 763 nm which also emits at night in a thin layer near 94 km, and finally OH which emits in a thin layer centered at 85 km. During the daytime the first two emissions are intensified by additional processes, and they are measurable against the background of Rayleigh and baffle scattering. The UARS requirement is for a measurement every minute, so if two different emissions are used, a complete measurement for one emission must be made in 30 s.

The principal objective is to provide global measurements of wind for comparison with current global circulation models (GCMs) and, in so doing, identify those processes responsible for wind forcing at these altitudes. The mesosphere is an important interface between the stratosphere, largely controlled by radiative processes, and the thermosphere which is controlled by a combination of photochemical and electromagnetic processes. It is thus influenced by forces from above and below. From above, the energy input into the aurora and the associated electric fields and currents drive the ions, which transfer momentum to the neutrals. This influence is well established in the  $F$  region where Doppler measurements have been made with the 630.0-nm atomic oxygen emission. What is not known is how low in the atmosphere the effect penetrates. Electrodynamic effects as well as auroral heating appears to launch gravity waves that move equatorward, producing heating effects that have been observed in the 630.0-nm emission at the equator. Some WINDII observing time will be allocated to investigating these effects, using the 630-nm  $O(^1D)$  emission for neutral winds and the 732- and 733-nm  $O^+(^2P)$  lines for ion winds.

From below, gravity waves produced near the Earth's surface propagate up to the mesopause region, where they "break" and interact with the mean flow. The influences from above operate in a frame of reference attached to the Sun, with dynamical perturbations that can be correlated with magnetic disturbances. The intensity of gravity waves propagating from below is determined by the forcing mechanism at the surface and the filtering due to the wind field in the intervening atmosphere. Variations, associated with these factors, in the observed amplitudes of these waves are expected to be observable and so should appear in the daily wind maps. The appearance of such daily patterns would constitute a major discovery and provide unambiguous evidence for coupling from the troposphere to the mesosphere.

On a smaller scale, the identification of the characteristics of individual gravity waves would be of great importance. Observations of the longitudinal, latitudinal, and seasonal variations would be very valuable. Observations of vertical gradients in horizontal wind variances would permit evaluation of momentum transfer and gravity wave breaking. Simultaneous measurement of the background winds will allow the breaking process to be investigated. Quite apart from the wind measurements, measurement of temperature and emission rate will be made; these also have gravity wave signatures. Here the capability of measuring rotational and Doppler temperatures will be of great interest. The long integrating paths at the limb will tend to smear out wave structures, but as yet we are unable to say to what extent the short wavelength wave will be observable.

Tides are another influence from below that need to be investigated [Forbes, 1982a, b]. As with gravity waves, they increase in amplitude with height and are thought to break in the lower thermosphere. While it is not clear that WINDII samples frequently enough over a large enough spatial region to unambiguously resolve the spatial variations of all the tidal modes, it will certainly contribute to investigations of their nature.

Volume emission rates permit the deduction of certain species concentrations, in particular atomic oxygen, although other species are of interest as well. This will allow studies of the transport of O, and direct correlations between

species concentrations, and their advection by the observed winds. From such a study, photochemical time scales may be derived and the coupling between the dynamics and the horizontal variations in species concentration investigated.

In addition to the primary mandate of UARS, individual team members have interests that extend well into the thermosphere, which is consistent with the UARS objectives that call for a study of coupling between regions. Optical measurements will necessarily detect aurora and give a measure of local energy input, supplemented by the particle environment monitor (PEM) measurements (particularly its X ray imager AXIS which views in the same direction as WINDII). Optical measurement of  $O^+$  gives ion winds, which in turn allow ion-neutral momentum transfer to be studied. Enhanced winds and convection near auroral forms are expected, since there is now considerable evidence for upwelling and atomic oxygen depletion near auroral forms. Although a thermospheric phenomenon, such depletions are likely to be one of the sources of variations in atomic oxygen and hence provide a mechanism for coupling between the thermosphere and the mesosphere.

#### 1.4. Characteristics of the WIND Imaging Interferometer (WINDII) Target Emissions

WINDII fundamentally measures the modulation of two line of sight interferograms for various emission features; from this modulation the apparent Doppler velocity, Doppler temperature, and emission rate are determined. The two data sets may be combined to provide a limited tomographic capability. Combining the emission rates for different spectral lines within a single molecular band allows rotational temperatures to be obtained as well [Mende *et al.*, 1988]. By inverting these data, vertical profiles of these same quantities are derived. However, because of the numerical procedures involved and the necessary assumptions for the analysis, the results from these inversions require a knowledge of the emission characteristics. Further quantities, such as the vertical profile of atomic oxygen concentration, may be determined from the volume emission rate profiles [Evans *et al.*, 1988]. From the concentration profile, the temperature profile, and the vertical wind gradient, it is possible to derive diffusivity coefficients. Table 1 lists both the directly measured and the inferred quantities.

The upper mesosphere/lower thermosphere emissions (the oxygen green line, the oxygen atmospheric band, and the hydroxyl vibration/rotation bands) are essentially confined to narrow layers in the altitude region 85–97 km. Thus the requirement of good definition for the emission height profiles demands that the pixel bins be selected so that they reflect this narrow height range. However, there are a number of observations [Swenson *et al.*, 1989] which suggest that the emission layer heights are not as constant as is often assumed, so that the limited height range sampled from the CCD must be selected to reflect these known variations. As the mesospheric emissions are known to exhibit wave structure, the full detailed analysis of the observations requires the stereoscopic capability afforded by the two WINDII fields of view.

Quantities that are measured by WINDII are emission rate profiles, wind profiles, and temperature profiles. Although the apparent properties are measured directly, they must be inverted to obtain the actual quantities. In order to properly

TABLE 1. WIND Imaging Interferometer (WINDII) Measured and Inferred Parameters

Quantity Measured	Conventional Method of Measurement
557.7-nm volume emission rate	rocket
557.7-nm wind	GB FP, GB WAMI, rocket,* radar
557.7-nm temperature	GB FP, GB WAMI
630.0-nm volume emission rate	rocket
630.0-nm temperature	incoherent scatter, GB FP, GB WAMI
630.0-nm wind	GB WAMI, GB FP, rocket,* radar
O <sup>+</sup> emission rate	GB scanning interferometer
O <sup>+</sup> wind	incoherent scatter radar
OH emission rate	GB FTS
OH wind	GB FP, GB WAMI, radar, rocket*
OH Doppler temperature	Lidar, rotational temperature
OH rotational temperature	GB FTS, spectral imager
O <sub>2</sub> atmospheric (atm) volume emission rate	rocket
O <sub>2</sub> wind	rocket,* radar, GB WAMI, HRDI
O <sub>2</sub> rotational temperature	GB spectral imager, rocket
Rayleigh scattering temperature	lidar, HRDI
Gravity wave characterization†	GB WAMI, radar, lidar
Diffusivity†	rocket
Atomic oxygen concentration†	rocket

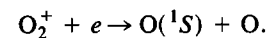
GB, ground based; FP, Fabry-Perot; FTS, Fourier transform spectrometer; HRDI, high-resolution Doppler imager; WAMI, some form of wide angle Michelson interferometer.

\*Radar chaff or chemical trails.

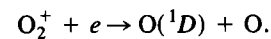
†Denotes inferred quantity.

interpret the results it is essential to have a knowledge of the emission processes. For example, it is important to recognize that all of the emissions used here are forbidden: in the mesosphere and lower thermosphere the emitting species suffer sufficient collisions between excitation and radiation, so that the emissions are characteristic of species in thermal equilibrium with the surrounding gas (radiative lifetimes are given in Table 2). In the middle thermosphere, where collision times are longer, this is not necessarily true. The various airglow emissions associated with the recombination of atomic oxygen originate from different altitudes in the atmosphere [Llewellyn and McDade, 1984]. Thus measurements of these different features can provide atomic oxygen concentrations at several different altitudes. Height profiles are possible through measurements of the OH Meinel bands, the O<sub>2</sub> atm (0-1) band, and the O<sup>1</sup>S green line. Characteristics of the emissions are given in Table 2, which apply to both daytime and nighttime.

There are two regions of excitation for the airglow, with recombination of the atomic oxygen layer causing excitation of the nightglow in the 100-km region and ionic recombination processes exciting emissions in the 150- to 300-km region. For example, at levels above 150 km the green line emission is excited by dissociative recombination:



Photoelectron fluxes from daytime ionization by solar EUV photons and electron fluxes from auroral precipitation enhance the ion production and excite the green line at intermediate levels from 100 to 200 km. The same processes excite O(<sup>1</sup>D), the upper state of the red line emission:



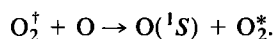
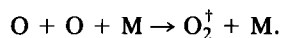
For the thermospheric emissions the quality of the WINDII data are such that it should be possible to extract any mesospheric component (e.g., as in the case of the O(<sup>1</sup>S) green line) and to identify the emission components that are excited in different ways. In particular, the oxygen red line is excited by both dissociative recombination and by photoelectron impact, in a process similar to that in the aurora. The dissociative recombination process can lead to hot atoms, with a large spectral line width, while the electron impact will give normal line widths. Thus the observations can be used to identify both the excitation impact cross section and the atomic oxygen profile. Below 150 km the O(<sup>1</sup>D) atoms are quenched by molecular nitrogen and oxygen to give the oxygen atmospheric band emission, an

TABLE 2. Emission Characteristics

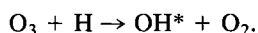
Emission	Lifetime, s	Wavelength, nm	Height Range, km	Peak Altitude, km	Half Width, km
O <sup>1</sup> S green line	0.8	557.7	lower 80-110 upper 150-300	97 200	15 50
O <sup>1</sup> D red line	110	630.0	150-300	~250	~100
OH (8-3) band	4.2 ms	730.0	80-110	87	10
O <sub>2</sub> atm (0-0) band	14	762.0	80-110	94	10
O <sup>+</sup> line	5	732.0	200-300	~150	~50
Green continuum		500-900	80-120	90	20
Rayleigh scattering		500-900	80-120	exponential falloff	

emission that is also studied with WINDII. Thus WINDII has the capability to make measurements of the  $O(^1D)$  population to lower altitudes than is normally possible.

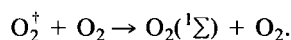
At lower levels the green line of atomic oxygen is excited by the reassociation of atomic oxygen in the atomic oxygen layer at 100 km and the subsequent energy transfer [McDade *et al.*, 1986]:



The hydroxyl emission originates from the recombination of the atomic oxygen layer into ozone and the subsequent reaction with atomic hydrogen to form vibrationally excited hydroxyl, which emits into numerous bands, including the (8-3) band observed by WINDII [Murtagh *et al.*, 1987]:



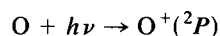
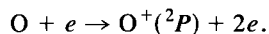
The recombination of atomic oxygen into molecular oxygen and the subsequent energy transfer can also lead to the excited electronic state,  $O_2(^1\Sigma)$ , which is the radiating state for the  $O_2$  atmospheric band emission:



$O_2(^1\Sigma)$  is also excited by energy transfer from  $O(^1D)$  in the day airglow; the  $O(^1D)$  is produced by ozone photolysis and by photodissociation of  $O_2$  and of  $H_2O$  by ultraviolet sunlight. There is also a daytime contribution to the atmospheric band emission from the resonant scattering of sunlight.

The interpretation and conversion of the measured quantities into meaningful geophysical quantities requires the knowledge of both the kinetic temperature and the atmospheric density in the emission region. The kinetic temperature is measured from the emission itself, but for the density we must use either a model, which is itself uncertain, or the absolute intensity of the Rayleigh scattering.

The high altitude  $O^+$  emission at 732.0/733.0 nm is excited mainly by EUV photoionization ( $\lambda < 67$  nm) during the day and in twilight, while at night, auroral electron precipitation can excite this species as follows:



Thus the daytime emission may be used to study the variation in the solar EUV output as well as atomic oxygen concentration [McDade *et al.*, 1991], extending the range of the solar spectrum monitored by UARS into the UV. Rayleigh scattering of sunlight by  $O_2$  and  $N_2$  occurs in the daytime and creates a continuum background in all channels at low altitudes. The intensity of this scattered light decreases exponentially with altitude with a scale height of about 7 km. Measurements of the intensity variation with altitude can be used to measure the temperature at lower altitudes, and the absolute values will yield a measurement of atmospheric total density.

The green continuum comes from the recombination of nitric oxide with atomic oxygen [Swenson *et al.*, 1985]:

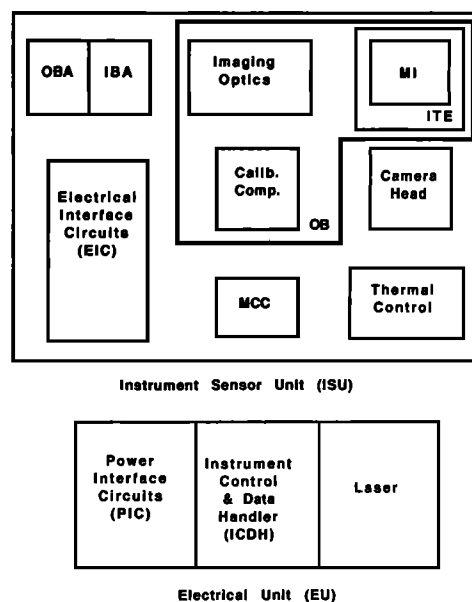
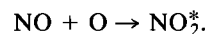


Fig. 2a. Block diagram of the WINDII system. OBA, outer baffle assembly; IBA, inner baffle assembly; MI, Michelson interferometer; MCC, mirror controller component; ITE, inner thermal enclosure; and OB, optical bench.



This emission is weak but contributes a significant signal in the wide band-pass background channels in the altitude region from 80 to 100 km.

During auroral events in the polar regions, energetic particle precipitation enhances most of these emissions and increases the brightness of the green line and red line emissions by manyfold. Thus auroral winds and temperatures may also be investigated.

## 2. DETAILED INSTRUMENT DESCRIPTION

### 2.1. Overview

The WINDII system consists of a flight segment (the instrument) and a ground segment (remote analysis computer (RAC)). The instrument is comprised of two units: the electrical unit (EU) and the instrument sensor unit (ISU). The ground segment consists of the RAC hardware, software, and network connections. A system level block diagram of the instrument is shown in Figure 2a and a drawing of the assembled physical system in Figure 2b.

The EU houses the microcomputer controller (instrument control and data handler (ICDH)), power regulation, conditioning and distribution circuits, interfaces with a UARS remote interface unit (RIU) for telemetry and command, interfaces with the UARS power supply unit (PSU) for quiet, pulse, and survival power busses, and the calibration laser. The ISU contains the outer and inner baffle assemblies, the imaging optics, Michelson interferometer, CCD camera, calibration component, mirror controller, electrical interface circuits, thermal control heaters, thermistors, thermostats, blankets and radiator plates, pyrotechnic devices, and interfaces.

In terms of operations the EU ICDH receives command data from the UARS RIU and executes daily experimental

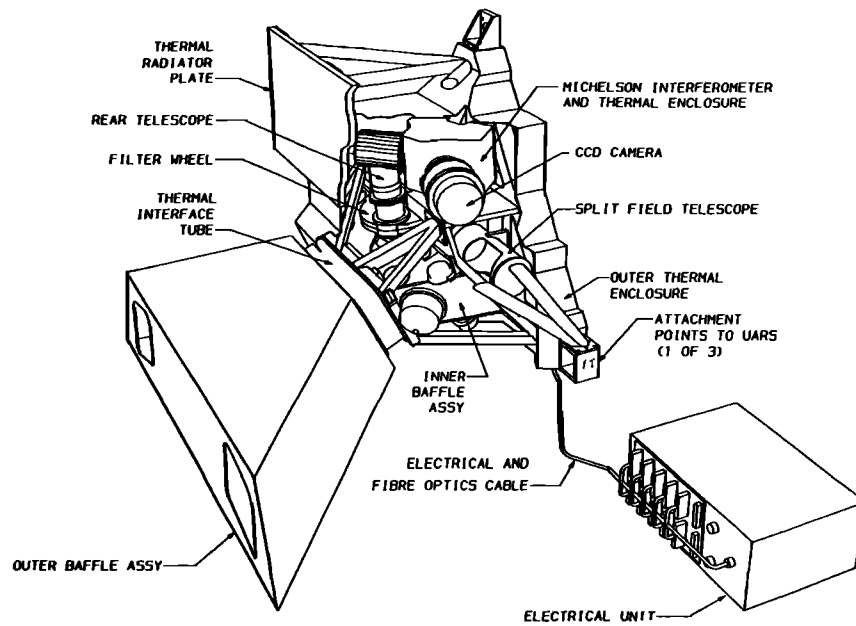


Fig. 2b. WINDII configuration. The two orthogonal input beams enter through the two ports on the left, in the outer baffle assembly, and cross over before entering the inner baffle assembly and then the split field telescope where the two inputs are combined into a single beam. This beam passes upward through the filter wheel and the rear telescope before entering the Michelson interferometer, in its thermal enclosure. The CCD camera is located immediately behind the Michelson interferometer. Calibration light is introduced at the circular ports on the inner baffle assembly by an optical fiber harness (not shown). The laser is located in the electrical unit, and the light is transported through a fiber optics cable along with the electrical cabling.

programs based on data tables updated by the uplinked commands. Telemetry containing image data and engineering information is formatted by the ICDH and transferred to the RIU for downlink using the 2000 bits/s allocation for WINDII. The experimental parameters for each measurement are determined by the flight software resident in the ICDH and are provided to the ISU on a bidirectional 1-MHz serial data link. This connection also allows the CCD camera data to be transferred to an image data buffer in RAM within the ICDH memory. A limitation on the amount of image data from a measurement of 20480 bins is based on the constraint of 32 kbytes of image RAM.

The ISU electrical interface circuits (EICs) act as a data distribution center as it receives instructions from the ICDH and passes them on to the appropriate component: mirror controller, camera controller, calibration component, or analog multiplexer. The mirror controller positions the scanning mirror of the Michelson interferometer at a specified position for each image. The camera controller provides the control signals to the CCD camera to clear the CCD, start an exposure, transfer the image to the storage area, read out the image using on-chip binning, digitize the video signal, and format the 12-bit data into 16-bit words for transmission on the 1-MHz data link back to the ICDH image memory. The calibration component responds to commands to select a specific lamp and provides optical output monitor analog signals. The analog multiplexer samples the output and temperature monitors from the calibration component and temperature sensors monitoring the thermal control and the CCD.

## 2.2. System Level Description

2.2.1. *Michelson interferometer.* The interferometer is similar in design to the one made for the earlier WAMDII

instrument [Shepherd *et al.*, 1985] but there are some important differences.

The beam splitter consists of two cemented half hexagons with a low-polarizing semireflecting dielectric multilayer [Dobrowolski *et al.*, 1985] on one of the diagonal faces. It is made of BK7 glass and the entrance and exit faces are 7.6 cm<sup>2</sup>. Both arms are solid glass (LF5 and LaFN21) except for a small gap at the end of the LF5 arm. The gap is necessary to allow the small mirror motion which is required to scan one or two fringes and also provides an extra degree of freedom in the design of the Michelson. A diagram of the Michelson optics is shown in Figure 3.

The moving mirror is cemented to three piezoelectric pillars which in turn are cemented to the end of the arm. The other mirror is coated directly on the end of the LaFN21 arm. All air/glass surfaces have antireflection coatings. The position and tilt of the moving mirror are sensed by three small capacitors consisting of electrodes deposited on the end of the LF5 arm and on the ends of glass pillars cemented

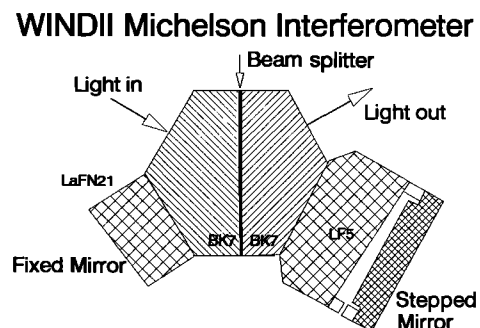


Fig. 3. Configuration of the Michelson interferometer.

to the mirror. These capacitors form part of a bridge which provides an error signal to the circuit that controls the voltage on the piezoelectrics. The interferometer's alignment and stepping are controlled by the computer through this system. The moving mirror assembly and control circuits were provided by Queensgate Instruments, United Kingdom. The beam splitter and glass arms were manufactured by Interoptics, Ottawa.

An optimum path difference exists for wind measurements for any given wavelength and line width, and since WINDII's suite of emissions includes both narrow lines near the mesopause ( $O_2$ , OH, OI 557.7) and broad ones from the thermosphere (O I 630.0, OI 557.7, O II 732.0/733.0 nm), a compromise had to be found. Optimum for the narrow emission lines occurs at very large path differences (greater than 10 cm), but then the fringe contrast for the broad lines is almost zero. Since atomic oxygen at 630.0 nm was considered one of WINDII's important targets, it was decided to limit the path difference to about 4.5 cm, a value which would allow good measurements of this emission. Although less than optimum for the narrow lines, an analysis showed that this choice would still allow more accurate wind measurements to be made for the narrow lines than for the broad ones and, in fact, should allow all target accuracies to be met.

A further complication is the complex nature of the OH,  $O^+$ , and  $O_2$  lines, whose components are too closely spaced to be isolated by interference filters. The path difference must be chosen so the phase difference between the component fringes does not seriously reduce the contrast of the resultant fringe. It was decided to attempt to match the phase of the two principal  $O_2$  lines,  $^P P(7)$  and  $^P Q(7)$ , on the ninth beat, at an effective path difference of  $D = 4.550$  cm (see (13)). The required arm dimensions were calculated from dispersion data provided by Schott for the pieces of glass to be used for WINDII. Calibration measurements using an  $O_2$  source later showed that the two fringes differ in phase by less than  $10^\circ$ , verifying the validity of the instrument model and the wavelength difference used. Matching the phase of the two fringes as closely as possible not only produces the best visibility but also gives the least change of phase if the relative intensities of the two component emissions change. The interferometer can be designed to produce such a condition for one pair of lines, but in practice one has to be very lucky for the same design to match the phase for other doublets. For example, the  $\Lambda$ -doubled components of the OH (8,3)  $P_1(3)$  line are  $80^\circ$  out of phase, reducing the visibility by 23%. But one can work with this, and the phasing for the  $P_1(2)$  components is much worse. At higher  $K''$  values the lines become more difficult to isolate and lower in intensity. The case for the  $O^+$  doublets is more favorable, as both are expected to have a phase separation of about  $25^\circ$ , giving a visibility reduction of no more than 6%. The filter function separates the two pairs of lines in the field of view, with 733.0 nm dominating near the center and 732.0 nm near the edge.

The Michelson is designed to have a large field of view and to be thermally compensated with respect to phase throughout the required spectral region of 552 to 763 nm. The thermal compensation is accomplished by balancing against the thermal coefficient of the scanning mirror mounting against that of the rest of the interferometer, in the way described by Thuillier and Shepherd [1985].

An important feature is the use of wedges in the interferometer to reduce the contrast of fringes caused by reflections at the air/glass surface in the LF5 arm. Such "secondary" fringes caused circular ripples to appear in the visibility and intensity images taken with the engineering model of the WAMDII instrument. In WINDII both the interferometer mirrors and the air/glass surface near the scanning mirror are slightly tilted with respect to the optic axis. The tilts (26–38 arc sec, greatly exaggerated in Figure 3) are calculated to reduce the contrast of the secondary fringes by a large factor while preserving the high contrast of the primaries. Measurements have shown that the instrumental visibility factor for the primary fringes is  $\sim 0.9$  (where 1.00 is perfect) and only a slight trace has been found of secondary fringes, and then only for visibility images taken with the daytime aperture, at a level of about 2.5%.

**2.2.2. WINDII optical system.** The principal elements of WINDII's optical system are a baffle, a telescope with two objectives and a field combiner, a filter wheel, another telescope, the Michelson interferometer, and the CCD camera. The two orthogonal fields of view, each  $4^\circ \times 6^\circ$  in object space, are imaged side by side at the detector. Inside the baffle, two mirrors are deployed during calibration to block the incoming light and allow the instrument to view the calibration sources. The optical train has been folded into a compact shape by means of several plane mirrors.

The main function of the baffle is to limit the amount of scattered light reaching the optics during daytime and to permit daytime measurements of the airglow. To achieve maximum baffle length within the allowed instrument envelope, the two fields of view are criss-crossed inside the body of the baffle. The last vane in each section is located at the aperture of the first telescope and behind the apertures are the fold mirrors that direct the light from the two fields of view toward the telescope's objective lenses. During daytime the entrance apertures are stopped down to a narrow slot shape parallel to the horizon and to the bottom edge of the first baffle vane. The first vane is so placed that for the average spacecraft altitude the scattered sunlight from clouds at the top of the troposphere is prevented from entering the aperture. The loss of the aperture area during daytime is partially compensated by the increased brightness of the emissions. The WINDII baffle is shown in Figure 4.

The first telescope accepts light from the two fields of view and combines them side by side into one field. The second telescope projects an image of the aperture at the Michelson mirrors and provides a real field stop for the reduction of scattered light. The filter wheel, containing eight positions, is located in the collimated light between the two telescopes.

Light passes next through the Michelson interferometer, which modulates the emission lines and provides the means to detect small wavelength shifts and to measure line widths. In order to prevent reflected light being recycled through the interferometer, it is tilted downwards by  $3^\circ$ . This causes light emerging from the forward output of the Michelson to be trapped at the field stop [Shepherd et al., 1985; Ward et al., 1985].

The CCD camera consists of an  $f/1$  "collector" lens which focuses an image of the field of view at the CCD detector. There is no shutter in the instrument, other than the calibration mirrors, and an exposure is ended by the rapid transfer of the image from the exposure area to the

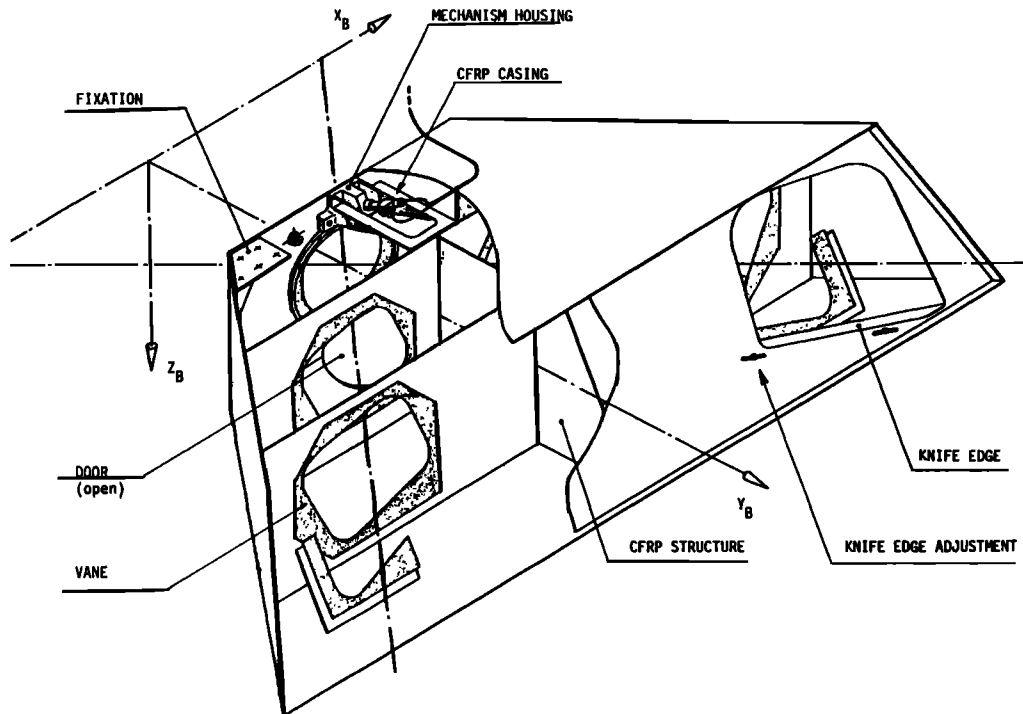


Fig. 4. Drawing of the outer baffle assembly. The optical axes entering through the two ports at the front are orthogonal and cross over through the single port at the back. The port was covered by a door during the launch phase. Note the knife edge at the top right, which was adjusted during alignment so as to shadow the daytime entrance aperture from the bright cloud tops.

storage area, from which it is read out while the next exposure is being made.

The same exposure and same filter must be used for both halves of the field of view, but the day/night apertures are individually controlled.

**2.2.3. Imaging optics.** The system comprises two telescopes in tandem followed by the Michelson interferometer and the collector optics, which focus the field of view at the CCD detector. The first telescope has two objectives directly opposed to one another. Symmetrically disposed between these objectives is a beam combiner, two orthogonal mirrors whose apex coincides with the two overlapping, intermediate image planes. While half of the image coming from each objective is discarded since it bypasses the prism without undergoing reflection, the remaining two halves are made to line up side by side. Following the beam combiner, the light is recollimated by the eyepiece before passing through the second telescope. The filter wheel is located in the collimated beam between the telescopes. The functions of the second telescope are to provide this space where a single filter wheel can be used for both fields of view and where the filters do not have to be excessively large and to provide a real field stop for the control of stray light.

The main requirements for the optics are as follows: (1) angular magnification, 1.43 in first telescope and 1.00 in second telescope; (2) focal length of collector optics, 50 mm; (3) aperture in object space, 68.5 mm; (4) field of view in object space,  $4^\circ \times 6^\circ$  for each channel side by side to correspond to an image format  $9.75 \times 7.31$  mm; (5) resolution at CCD array, modulation transfer function (MTF) across entire image to exceed 35% for 12 line pairs per mm; (6) distortion, not to exceed 2.5%; (7) vignetting at corner of field, not to exceed 30%; (8) spectral range, 550–770 nm; (9)

aperture stop location, mirrors of the Michelson interferometer; and (10) design to accommodate mirrors for folding and combining the optical paths.

The scale drawing in Figure 5 is the final design for the imaging optics of the WINDII instrument in its unfolded state. Because of the relatively high effective aperture and small field size associated with the objective of the first telescope and the eyepiece of the second, both these lens groups have a Petzval type of construction. The other two lens groups in the foreoptics have a triplet derivative construction and, in fact, are identical. The collector optics at

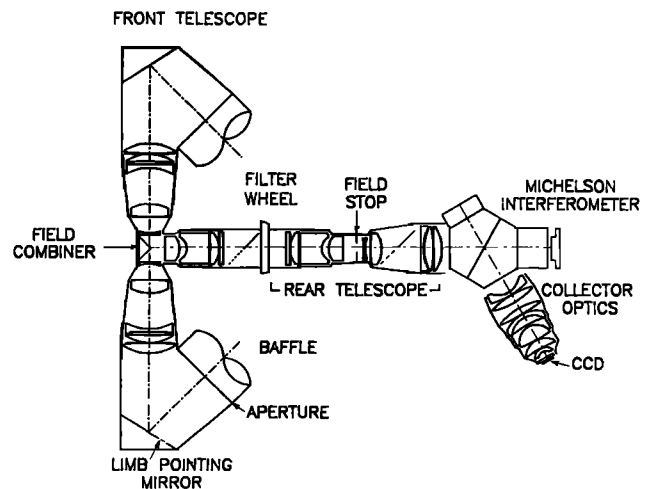


Fig. 5. Schematic diagram of the optical system. Most of the elements can be identified in the actual configuration shown in Figure 2b.

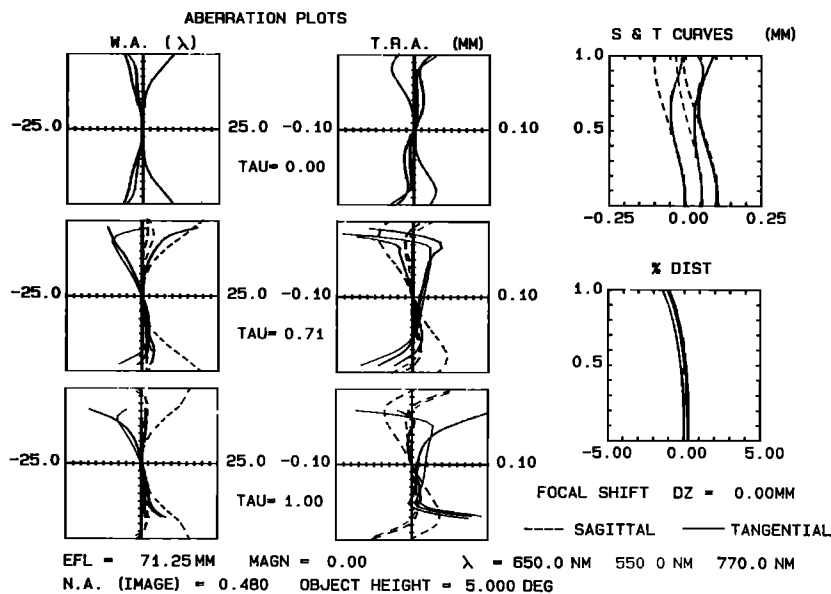


Fig. 6. Wave front aberrations in the imaging optics.

the rear, which focuses the light at the CCD array, has a numerical aperture of  $f/1.0$  and a stop located at the mirrors within the Michelson, 125-mm air equivalence from the lens group's first element. The design of this lens group was significantly more challenging than that of the foreoptics, but experience gained from the WAMDII project [Powell, 1986] allowed us to avoid the usual exploratory stage by utilizing the collector optics design from that instrument as a starting solution for this design. After the design of each individual lens group was completed, the system was optimized as a unit and the illustrated configuration evolved.

The overall system was analyzed for three field points and the wavefront and transverse ray aberrations are illustrated in Figure 6. As is often found in complex optical systems, some residual longitudinal secondary chromatic aberration is present. Fortunately, since the system operates only in

narrow bandwidths at any one time, this aberration can be overcome by incorporating a certain amount of power into the appropriate interference filter. This results in the performance remaining nearly constant over the entire spectral range. This can be seen from Figure 7 which depicts MTF plots associated with the central and extreme wavelengths for the appropriate amount of correction. Reduced spatial frequency,  $s$ , in the plots is related to real spatial frequency,  $N$ , by the equation  $s = N\lambda/na$ , where  $na$  is the numerical aperture. Even at the short wavelength where the MTF drops off more rapidly, the MTF at the extreme off-axis field point for a real spatial frequency of 17.5 line pairs per millimeter (corresponding to 0.02 reduced spatial frequency) is around 30%.

2.2.4. *CCD camera.* The WINDII detector consists of a CCD camera with an  $f/1$  lens and a thinned, back-

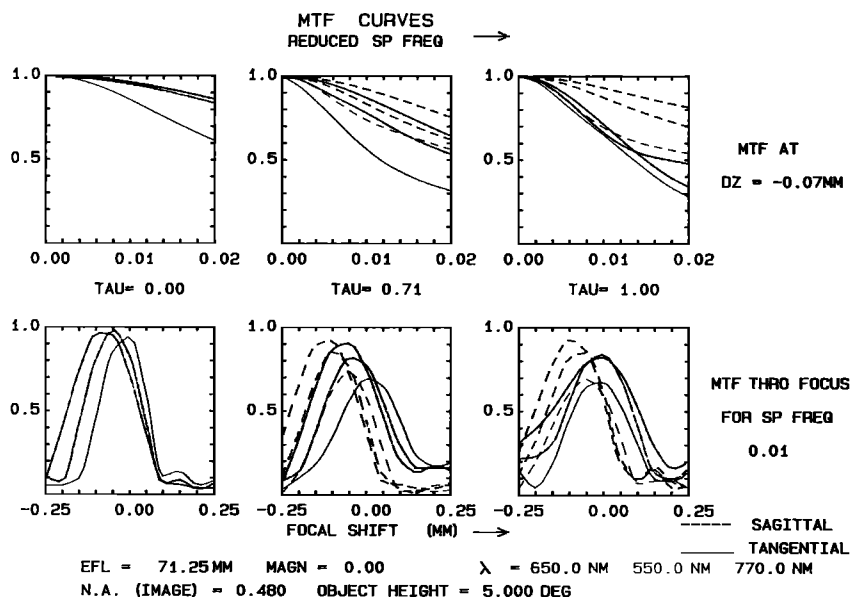


Fig. 7. Modulation transfer function (MTF) plots for the imaging optics.

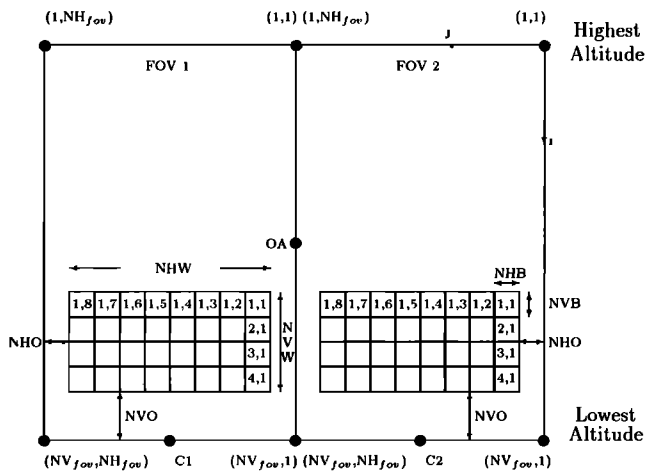


Fig. 8. Schematic diagram of the bin and window placement on the CCD for a typical measurement. The bins are numbered from the top right corner of each field of view since this is how they are read off the detector. Each bin is composed of NVB by NHB pixels and each window is composed of NVW by NHW bins. The windows are offset vertically, NVO bins, and horizontally, NHO pixels. The maximum size of a field of view is  $NH_{fov} \times NH_{fov}$  pixels or  $256 \times 160$  pixels. C1 and C2 are the boresight locations for each field of view and OA is the location of the imaging optical axis. Light which is normally incident on the Michelson optics is imaged at the bottom center of the CCD, below OA and half way between C1 and C2 at the juncture of the two fields of view.

illuminated CCD, RCA part number SID501 EX. The pixel elements are about  $30 \mu\text{m}^2$  and the device consists of  $512 \times 320$  pixels. In the WINDII application, one half of the array is used as storage and is masked off to avoid illumination. The mask is actually extended 10–12 rows into the imaging area to ensure that illumination does not reach the storage area.

The image area then consists of 256 rows and 320 columns. Because of the two fields of view (FOVs) in WINDII the image area is further divided in two so that 256 rows and 160 columns are used for each FOV. Thus the two FOVs are imaged side by side on the CCD image area, as shown in Figure 8.

The camera is operated using firmware. Exposure sequences are commanded by the central microprocessor (ICDH) and interpreted by the camera controller.

The measurements are specified in terms of the bin dimensions, vertical and horizontal window size, vertical and

horizontal offsets from the bottom and outside edges, and the vertical separation between displaced windows if this is required.

At the end of an exposure the entire image area is transferred quickly (about 3 ms) into the storage area where it is read out according to the measurement specifications. Rows which are not part of the measurement window are flushed out and the vertical and horizontal binning performed during the readout operation for all rows within the window of interest. Once all the charge associated with the pixels within a given bin are accumulated in the output storage register, the voltage is sampled and digitized.

The output storage register has a full well charge capacity of 300,000 electrons and the voltage is digitized into 12 bits resulting in a nominal resolution of 73 electrons/count. The electronic readout noise of the CCD and the subsequent analog chain is about 100 electrons rms, so that a signal level of 10,000 electrons yields a signal to noise ratio of 100. A fixed analog bias of about 100 counts is added to the video signal.

Between measurements the CCD is operated in idle mode with the entire CCD flushed every 128 ms. Just prior to each exposure the CCD is quickly flushed 4 times. Exposures are timed precisely using a crystal oscillator.

The CCD is kept at operating temperature ( $-45^\circ$  to  $-55^\circ\text{C}$ ) by a pair of two-stage thermoelectric coolers (TECs). The heat rejected by these TECs is conducted out of the camera and to a radiator plate. The operating temperature is affected by the radiation input to this radiator plate which is dependent on the Sun angle and the albedo from the Earth. The temperature of the CCD is monitored by a thermistor mounted as close as possible to the CCD. This thermistor is sampled during every image and the temperature value inserted into the telemetry.

**2.2.5. Optical filters.** The function of the filters is to isolate, to the greatest extent possible, the atmospheric emission lines chosen for study. A summary of the filter parameters is given in Table 3. The filter wheel has eight positions, one of which is unfiltered and is used for viewing star fields and the calibration sources (which have their own filters). Filter 5 is a double filter, transmitting two spectral passbands simultaneously, so the filter wheel contains eight filters in seven positions. Two of the filters are used for measuring the intensity of the background continuum and have their passbands located adjacent to emission features in different parts of the spectrum. Six filters are devoted to the emission lines themselves.

TABLE 3. WINDII Optical Filters

Filter No.	Emission	Line Wavelength, nm	Central Wavelength Normal Incidence, nm	Bandwidth FWHM nm
1	background		553.1	1.6
2	O $^1S$	557.73	558.4	1.6
3	O $^1D$	630.03	630.7	2.7
4	O $^+ ^2P$	732.0/733.0	732.9	1.4
5A	OH $P_1(2)$	731.63		
5B	band		728.8	16.3
6	background		714.8	11.0
7	OH $P_1(3)$	734.09	734.6	1.2
	O $_2$ $^P P(7), ^P Q(7)$	763.22, 763.	763.2	0.09

FWHM, full width at half maximum.

Filters 2 and 3 are straightforward, as there are no other significant emissions nearby that could contaminate the measurements. Filter 1 is used to measure the background emission for both of these filters. Plate 2 shows the transmittance of filter 3 at the atmospheric line wavelength 630.0 nm, over the image area of the CCD. The source was a tungsten lamp coupled to a spectrometer set to that wavelength, and the transmittance over the upper part of the image where the 630-nm emission occurs varies from about 56 to 70%.

Filters 4, 5, and 6 are used for OH, which occupies a narrow strip along the bottom of the field of view. Because all the OH lines are closely spaced doublets due to  $\Lambda$  doubling, two sets of fringes are present and the phase difference between them is important in determining the degree to which the doublet is modulated by the Michelson. The known parameters of the Michelson predict that the  $P_1(3)$  line will be about 75% modulated. It is also the brightest line in the  $P$  branches at the average temperature of the OH layer and is easier to isolate than the only competing candidate,  $P_1(4)$ . Thus  $P_1(3)$  was selected for the wind measurement, and Filter 6 is dedicated to this emission line. The filter must transmit  $P_1(3)$  to the greatest extent possible while strongly rejecting the nearby OH lines. The shift of the passband with angle adds difficulty to this problem, but by adjusting the tilt of the filter in its mounting, it has been possible to provide adequate filtering for the  $P_1(3)$  line across most of the bottom of the field of view.

Filter 5 consists of two semicircular filters, denoted 5A and 5B, on the same circular substrate; 5B has a wedge prism cemented behind it which deflects its image by  $1.9^\circ$  in the field of view. Filter 5 thus produces two images simultaneously on the CCD, with the image for 5B appearing  $1.9^\circ$  above the image for 5A. Filter 5A has a broad passband which includes nearly all of the OH band and is used for determining the intensity profile of the OH layer. Filter 5B measures the intensity of the background continuum just shortward of the (8,3) band.

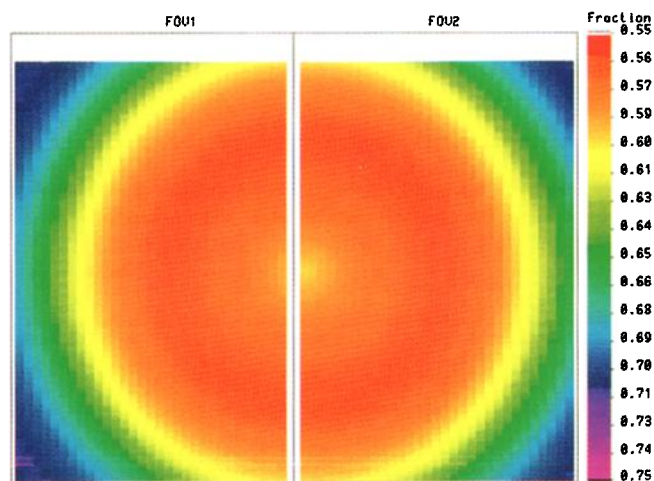


Plate 2. An image that simulates the transmittance of filter 3 to the atmospheric atomic oxygen 630.0-nm line. This information is required to determine the true (absolute as well as relative) emission rate for this emission. This image is obtained by dividing two measurement images of a screen illuminated with narrow-band 630-nm radiation generated by a monochromator, one with the filter in place, the other without.

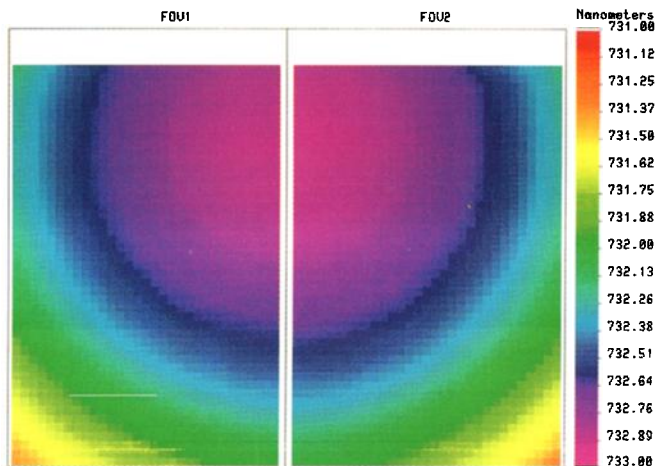


Plate 3. A map of the location of the filter passband peak over the CCD for filter 4, derived from a series of images taken during the stepping of the source monochromator. The  $O^+$  732.0- and 733.0-nm lines are transmitted at the top of the image (at high altitudes) and the OH  $P_1(2)$  line at 731.63 nm is transmitted at the bottom of the image, corresponding to 85 km altitude.

By a fortunate coincidence the wavelengths of the  $P_1(2)$  line of the (8,3) band and the  $O^+$  lines are such that one filter can be used for both emissions. Filter 4 is mounted in the filter wheel with an upward tilt of  $1.8^\circ$ , which allows it to transmit a mixture of the two  $O^+$  doublets in the upper half of the field of view. The shift of the passband with angle to shorter wavelengths allows  $P_1(2)$  to be transmitted at the bottom. The variation of passband peak wavelength over the image area of the CCD is shown in Plate 3; the color bar here corresponds to wavelength and varies from about 733.0 nm at the center of the ring pattern to 731.5 nm at the bottom corners. In practice, OH and  $O^+$  will not be observed simultaneously because the  $O^+$  appears only in the daytime, when it is expected that Rayleigh scattering in the lower part of the field will prevent the measurement of OH. The chief interest in  $P_1(2)$  is its sensitivity to rotational temperature (section 3.1.2.). It will not be strongly modulated by the Michelson, but that is unimportant in determining the intensity of the emission.

The (0,0) atmospheric (atm) band of  $O_2$  occurs in the bottom quarter of the field of view. Filter 7 is tilted  $3.6^\circ$  toward the bottom of the field to reduce the range of angles of incident rays. The  $P$ -like branches of the band have lines arranged with alternate spacings of about 0.3 and 0.1 nm and separating these lines requires a filter with a very narrow passband. The one chosen for  $O_2$  is a single cavity filter with a bandwidth of 0.09 nm and a peak transmission of 0.45. With such a narrow passband the wavelength shift with incident angle strongly affects the transmission pattern in the field of view. Individual lines appear in broad rings centered on the location in the field corresponding with the direction of the normal to the filter. The  $^P P(7)$  and  $^P Q(7)$  lines are blended and occupy about half the width of the field in the central region. The  $^P P(5)$  and  $^P Q(5)$  lines are also blended and are transmitted in a ring near the side edges of the field. Between these is a region of relatively low transmission. Measurements using filter 7 require a special algorithm to sort out the different contributions. The variation due to the filter in the relative weighting of the observed lines across

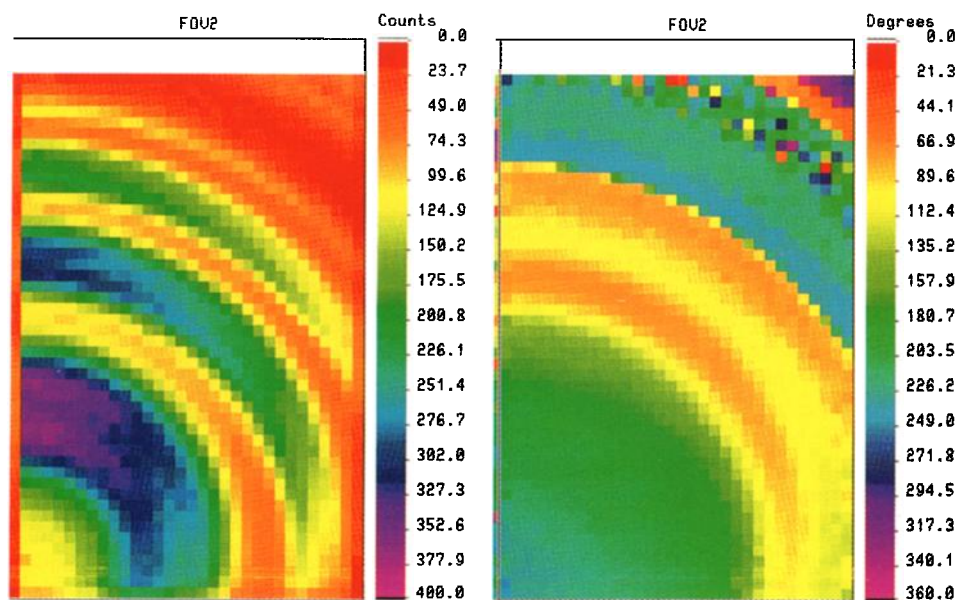


Plate 4. (a) The intensity image of a laboratory source of the  $O_2$  atm band emission and (b) the associated phase image. The circular rings correspond to different rotation lines in the (0,0) band.

the field of view is used to separate their contributions to the interferogram so that apparent quantities for each emission line are generated from each row in the image. The wind may be calculated from these apparent quantities in the same manner as with the simpler emissions and a rotational temperature may be estimated from the emission rate ratio of these lines. Plate 4a shows the intensity image obtained from a laboratory source of  $O_2$  atm band emission. Beginning near the bottom left and moving out, one can see three pairs of rotational lines,  $^P P(7)$  and  $^P Q(7)$  lines (mauve), then  $^P P(5)$  and  $^P Q(5)$  (dark blue) followed by  $^P P(3)$  and  $^P Q(3)$  (green). The  $^P P(1)$  line farther out (yellow) is not doubled. Plate 4b shows the corresponding phase image. The phase varies more slowly over the image than the intensity but can sharply change from one line to another resulting from the wavelength change. The Michelson interferometer was designed to have the  $^P P(7)$  and  $^P Q(7)$  closely in phase, which can be seen to be achieved.

**2.2.6. The calibration package.** The calibration of the instrument made in the laboratory before flight consisted mainly of measuring the following for each atmospheric line to be observed, the instrument responsivity, the interferometer intrinsic visibility, and the interferometer intrinsic phase. The first two of these quantities are expected to change slowly with time, on the ground before launch and in orbit. They are monitored in orbit on a weekly basis. The third quantity, the intrinsic phase, was expected to drift more rapidly as a consequence of temperature changes in the instrument; calibration for this is done every 20 min or so. A set of calibration sources is included inside the instrument to monitor both kinds of changes. Their use is based on the following: Calibrations from the ground-based sources are transferred to the on-board sources during the laboratory calibration so that they then constitute secondary reference standards. Following the laboratory calibration, any change in instrument characteristics is assumed to be determined from the data generated by the instrument calibration sources.

The instrument was calibrated using an external absolute standard (a tungsten ribbon lamp). This made it possible to calculate the instrument responsivity  $R_\lambda^0$  which converts instrument counts into rayleighs. Immediately after that measurement a similar source incorporated in the instrument generated a signal  $S_\lambda^0$  for each filter. In orbit this source will deliver a signal  $S_\lambda$  which will indicate that the instrument responsivity is then  $R_\lambda^0 S_\lambda / S_\lambda^0$ .

The on-board calibration source is a tungsten ribbon lamp contained in a vacuum-fused silica bubble. The current is regulated to within  $10^{-3}$  which provides a stability of the luminous flux of about 1%. The lamp is powered at  $5 \text{ \AA}$  and requires 6 W. The aging of the lamp intensity was monitored over a period of 6 months. For the best lamp chosen for the flight unit, a change of less than 5% was observed.

In section 1.1 the influence of the instrument on visibility was neglected, but the real interferogram involves the product of the line visibility  $V$  by the instrument visibility  $U$ .  $U$  is a smooth function of wavelength. In space the interferometer visibility may slightly change due to the action of the environment (particles and vacuum in which the cement may sublimate slowly). The visibility of the instrument as a function of wavelength was determined on the ground by using a laser capable of emitting at four wavelengths across the spectral region covered by WINDII. Consequently, monitoring the interferometer visibility at one wavelength during the mission has been considered adequate for the WINDII instrument.

For an emission line of unit visibility the interferogram provides the instrument visibility as shown by (3) of section 1.1. Under such conditions the width of this line is much smaller than the interferometer free spectral range. With about 45 mm optical path difference, only a laser can meet this requirement. We have chosen a He-Ne laser at 632.8 nm because its wavelength is in the middle of the instrument wavelength range. In addition to meeting the requirements of the space environment, the laser needs to be stable in intensity and wavelength during the calibration sequence (20

TABLE 4. Atmospheric Lines and Associated Calibration Lines for In-Flight Phase Calibration

Atmospheric Lines		Calibration Lines	
$\lambda_0$ , nm	Species	$\lambda_c$ , nm	Species
557.7	O <sup>1</sup> S	557.0	Kr
630.0	O <sup>1</sup> D	630.4	Ne
734.1/736.9	OH	738.4	Ar
732.0	O <sup>+</sup> <sup>2</sup> P	738.4	Ar
763.1	O <sub>2</sub> b <sup>1</sup> Σ	763.5	Ar

min). Several considerations have led to the requirement of a maximum of 1% change in intensity and  $10^{-9}$  in wavelength. The laser has been manufactured by QUANTEL. Its description and performance are given by *Thuillier et al.* [1992].

The measurement of the wind speed requires that one know the instrument intrinsic phase  $\phi_0$  for each atmospheric line to be observed. The determination of  $\phi_0$  is a two-step process. During ground characterization the phase  $\phi_0$  of laboratory sources emitting the atmospheric lines were compared with the phases  $\phi_c$  of the corresponding on-board spectral lamps. The space environment is expected to alter  $\phi_0$ , but difference  $\phi_0 - \phi_c$  are not expected to change between ground and orbit. Thus a measurement of  $\phi_c$  in orbit provides the required  $\phi_0$ , which we call the zero-wind phase. These data have to be known with an accuracy better than  $10^{-2}$  radian. Ideally, these on-board sources should emit at the same wavelength as the atmospheric line, but since the ground-based atmospheric line sources are not suitable for flight, we have chosen spectral lamp lines that are as close as possible to the atmospheric lines. They are shown in Table 4.

The gas is contained in a small fused silica bubble of 20-mm diameter and 15 mm long, having electrodes placed outside. They use a high-frequency (4 Mhz) power supply. The line is selected by a narrow-band interference filter. The lamps were manufactured by OPTHOS, in the United States.

The following sources are used: one He-Ne laser, one tungsten ribbon lamp, one Ne lamp, one Kr lamp, and two Ar lamps. In front of each source an optical fiber bundle collects the light. All fibers are randomly arranged. The optical cable bundle delivers the light to the instrument according to the required calibration sequence by switching the source to be used one or off.

### 2.3. Sensitivity

The sensitivity is best described by what we call responsivity, the ratio of the output signal to the input source strength. The output signal for WINDII is expressed in digitization levels called analog to digital units (ADUs); 1 ADU is equivalent to 73 electrons stored in the CCD bin. Airglow emission rates are traditionally measured in rayleighs ( $R$ ); one  $R$  corresponds to the emission of  $10^6$  photon  $s^{-1}$  from a  $1 \text{ cm}^2$  column extended along the line of sight. Put differently, it is the integral of the volume emission rate along the line of sight, and so it is the natural unit for input source strength. The responsivity can then be calculated in (ADU/s)/ $R$  as

TABLE 5. WINDII Error Estimate Parameters

Parameter	Value
Exposure error	0.03%
Step size error	0.03%
Dark current	30 electrons $s^{-1}$ pixel <sup>-1</sup>
Readout error	100 $e$
Digitization	75 electrons ADU <sup>-1</sup>
Quantum efficiency	0.55 to 0.23
MI efficiency	0.47
Average filter transmission	0.4
Lens/mirror transmission	0.75
Solid angle	$1.78 \times 10^{-7}$ sr pixel <sup>-1</sup>
Aperture area	32.7 $\text{cm}^2$
Aperture factor, night	1.0
Aperture factor, day	0.11

MI, Michelson interferometer.

$$R = \frac{1}{73} \frac{10^6}{4\pi} A \Omega \tau q \quad (14)$$

where  $A$  is the area of the input aperture,  $\Omega$  is the solid angle corresponding to one pixel as seen from that aperture,  $\tau$  is the overall system transmission, and  $q$  is the quantum efficiency of the detector. The responsivity is nearly the same at all wavelengths and is roughly  $5 \times 10^{-3}$  ADU  $s^{-1}$  Rayleigh<sup>-1</sup> for a  $1 \times 5$  pixel bin using the nighttime aperture and about a factor of 10 less for the daytime aperture. For filters 5A and 5B these numbers must be divided by 2 since each filter occupies only one half of the aperture.

### 2.4. Noise

A model of the instrument was used to define the requirements for the design of the instrument. The parameters needed for the model are given in Table 5. These are of three types. The first type consists of deviations from the ideal, such as errors in exposure time. The second type are parameters such as quantum efficiency which are fixed once the detector is selected. The third, such as the physical size of the aperture, is something that can be chosen, with certain limitations. These values were input to a model, along with estimates of the emission temperature and emission rate, assumed bin size, and exposure time, as indicated in Table 6. These estimates use our current knowledge of values for bin size, exposure time, dark current, readout error, quantum efficiency, and transmittance along with our prelaunch estimates for emission rate. In orbit we have found the emission rates to be extremely variable, so these should be taken as nominal errors. The computed wind and temperature errors are shown in the same table; these are errors in the apparent measurements. The errors following inversion to true height profiles, using in-orbit data, are described in section 4.2.

## 3. INVERSION AND TECHNIQUES FOR ANALYSIS

### 3.1. Methods and Concepts

3.1.1. *Data processing for apparent quantities.* Analysis of WINDII data begins at the level of the individual bins which compose the phase images. Figure 8 shows the layout of bins on the CCD array detector. Each bin measures a line of sight radiance (integrated emission rate) of the airglow limb. The altitude associated with a bin is the altitude at the

TABLE 6. WINDII Error Estimates

	Emission Characteristics and Conditions				Error Estimate	
	Temperature, K	Brightness, kR	Bin Size, pixels	Exposure, s	Wind, m/s	Temperature, K
			<i>Night</i>			
O I 5577	200	5	2 × 25	2	5	18
O I 6300	1200	5	6 × 25	2	6	20
OH 7341	200	1.5	2 × 25	4	10	50
O 2 7632	200	20	3 × 10	2	8	75
			<i>Day</i>			
O I 5577	800	25	4 × 25	1	12	40
O I 6300	1200	30	8 × 25	1	8	30
O II 7320	3000	5	8 × 25	1	75	N/A
O 2 7632	200	200	3 × 10	2	6	55

tangent point. Thus a column of bins scans a vertical slice in the atmosphere with an altitude range defined by the bottom and top bins in the column. The horizontal extent is normally the full width of the image area, which maps to about 140 km at the tangent points along a row of bins. Measurement bins are typically 25 pixels wide and 2 to 8 pixels high. A single pixel subtends approximately 1 km<sup>2</sup> at the tangent point giving a typical vertical resolution of 2 km. The bin size is optimized to give the best signal to noise ratio and best spatial and temporal resolutions possible for a given observation.

As discussed in section 1.1, the interferogram contains the atmospheric signal as well as a background signal. During normal operations a background image is taken followed by a set of phase-stepped images. Also, at 10- to 15-minute intervals a dark current image and calibration phase-stepped images are taken in what is termed a frequent phase calibration. The processing software subtracts the appropriate dark current from the background and atmospheric images bin by bin. The raw count rate is next converted to geophysical units (Rayleigh) using the measured responsivity of each bin. This calibration information is stored in a characterization data base (CDB) which is accessed by the production processing software. Since the background is taken at a different wavelength than the atmospheric line of interest, the current background image, following dark current subtraction, is corrected to the observation wavelength. The wavelength correction involves a knowledge of the background and filter bandwidths and the shape of the background light spectrum. At night the primary background sources are starlight and the NO<sub>2</sub> continuum. We have assumed that these spectral distributions are completely flat over the 5- and 14-nm separations between the background and the atmospheric filter passbands for the 557.7 and OH measurements, respectively, owing to the lack of more definitive information. The 630-nm filter is separated from its background measurement by 100 nm, but the NO<sub>2</sub> continuum is not a problem for the *F* region, and the starlight level is too small to be influenced by the above assumptions. During the daytime, one primary source is the baffle-scattered light from the cloud tops, which has the spectrum of sunlight (we neglect the spectral influence of the scattering), and the second primary source is Rayleigh scattering from the atmosphere within the field of view. The first source has a rather flat spectrum, and the second a  $\lambda^4$  dependence, but over the 5-nm separation involved for the 557.7-nm

emission this makes little difference. For the 630-nm emission the measurements are made in the *F* region where only baffle-scattered light is important, so a solar spectrum is assumed. Based on these assumptions, the background image taken immediately prior to the atmospheric measurement sequence is wavelength corrected and subtracted from each measurement image on a bin by bin basis.

WINDII is limb viewing and so is sensitive to the spacecraft attitude. (Star observations are taken from time to time to ensure accurate attitude knowledge, as described in section 5.2.) The altitude of each bin in each image is computed. Either 4 or 8 phase-stepped images are taken for a normal measurement. The observatory may roll or change attitude from image to image. Using the middle image in a set of 4 or 8 to give a reference altitude, the remaining images are corrected to account for any attitude variation. Next the velocities projected along the line of sight, due to spacecraft motion and Earth rotation, are derived for each bin. These are used to calculate the contribution to the observed phase of the spacecraft-induced Doppler shift. The instrument phase determined from the frequent phase calibration is corrected from the CDB to give the zero wind phase for the current measurement. Finally, the projected velocity phase and the zero wind phase are combined with the mirror step phase to give the known phase component of the measurement.

From (4) the integrated emission rate for a given bin at a given time may be written in the generalized form as

$$I_p = A(t_p) \int_L E(z) [1 + U_p V(z) \cos(\Phi_p + \phi(z))] dl \quad (15)$$

where  $A(t_p)$  is a trending function used to account for structure in the images.  $E(z)$  is the volume emission rate at altitude  $z$ .  $U_p$  is the intrinsic visibility of a given bin as determined through characterization; the value for WINDII is  $\sim 0.9$ .  $V(z)$  is the line visibility corresponding to the atmospheric temperature at altitude  $z$ .  $\Phi_p$  is the phase due to OPD, spacecraft velocity and mirror position is equal to  $2\pi x/\lambda$  in (4). The  $\phi(z)$  is the phase due to the atmospheric wind and  $l$  is the path length along the line of sight. Index  $p = 1, 2, \dots, n$ . This assumes  $n$  data points were taken for the measurement. If the cosine argument is expanded, then (15) may be written as

$$\begin{aligned}
I_p &= A(t_p) \int_L E(z) dl \\
&+ A(t_p) U_p \cos \Phi_p \int_L E(z) V(z) \cos(\phi(z)) dl \\
&- A(t_p) U_p \sin \Phi_p \int_L E(z) V(z) \sin(\phi(z)) dl \quad (16)
\end{aligned}$$

$$I_p = A(t_p) J_1 + A(t_p) U_p \cos \Phi_p J_2 - A(t_p) U_p \sin \Phi_p J_3 \quad (17)$$

The values  $J_1$ ,  $J_2$ , and  $J_3$  are the line integrals in (15) and they contain the atmospheric information we wish to recover. These values, originally defined in (9)–(11) are termed the apparent quantities.

Spatial gradients in atmospheric constituents may arise from gravity wave activity or from planetary scale dynamics. Spacecraft motion between successive images in a measurement sequence will therefore induce variations in the  $I_0$  of (4). There is no way to distinguish beforehand the scale of the disturbance, hence, we introduce a simple quadratic expression as a trending function which will accommodate local near-linear gradients. With this approach we cannot deal with short (i.e., 50 km) horizontal wavelength gravity waves, however, experience has shown that this is not a problem, probably because of the long integrating paths. The quadratic is expanded in pseudotime,  $t_p$ , which is really space when the spacecraft velocity is considered.

Thus we write  $A(t_p) = a_0 + a_1 t_p + a_2 t_p^2$ :

$$\begin{aligned}
I_p &= a_0 J_1 + a_0 J_2 (U_p \cos \Phi_p) - a_0 J_3 (U_p \sin \Phi_p) \\
&+ a_1 J_1 (t_p) + a_1 J_2 (U_p \cos \Phi_p t_p) \\
&- a_1 J_3 (U_p \sin \Phi_p t_p) + a_2 J_1 (t_p)^2 \\
&+ a_2 J_2 (U_p \cos \Phi_p (t_p)^2) - a_2 J_3 (U_p \sin \Phi_p (t_p)^2) \quad (18)
\end{aligned}$$

This may be written as a linear system of equations

$$I_p = \sum_{q=0}^{N_{\text{term}}} b_q X_q(U_p, \Phi_p, t_p) \quad (19)$$

where the  $X_q$  are the bracketed terms in (18). The  $X_q$  terms contain known information from the instrument calibration and the spacecraft attitude, while the  $b_q$  contain the atmospheric information.

Standard matrix techniques may be used to solve this linear system such as multiple linear regression (MLR) or a least squares multipoint algorithm (MPA) [Bevington, 1969]. Wave motion in the atmosphere perturbs the image data and when this is detected, horizontal rows of bins are combined to remove the wave component. The combination of a row of bins can be cast in the same form as equation (19). The solution for the  $b_q$  is improved by accounting for the curvature of the limb as seen across a row of bins. Also different forms of  $A(t_p)$  may be used to reduce systematic variations in the images.

The final result of either the MPA or the MLR solutions is to provide column vectors referenced to the centers of each

field of view for each of  $J_1$ ,  $J_2$ , and  $J_3$ . These are the apparent quantities that are input to the inversion routine.

3.1.2. *Rotational temperature measurement.* In addition to the measurement of temperature from the visibility, as described in section 1.1, WINDII is also capable of measuring rotational temperature for the two molecular emissions which it observes. This capability arises from the fact that in thermal equilibrium the intensity  $I_{J',J''v',v''}$  of individual emission lines within a band ( $v' - v''$ ) depends on temperature.

$$I_{J',J''v',v''} = N_{v'} Q_r(T) A_{J',J''v',v''} (2J' + 1) e^{-hcF(J')/KT} \quad (20)$$

where  $N_{v'}$  is the population of the upper vibrational level,  $Q_r(T)$  is the rotational partition function,  $A_{J',J''v',v''}$  is the Einstein transition probability, and  $F(J')$  is the rotational energy of the upper state  $J'$ .

For the (O,O) atmospheric band of  $O_2$ , (20) can be applied directly to determine the apparent temperature from the ratio of the line pairs  ${}^P P(7) + {}^P Q(7)/{}^P P(5) + {}^P Q(5)$  observed simultaneously in filter 7 images.

Derivation of hydroxyl rotational temperature is, in principle, the same but is made more complex because more than one filter is involved. As described in section 2.2.5, filters 4–6 select different wavelength regions of the hydroxyl (8-3) band emission. Filter 4 isolates the  $P_1(2)$  line, filter 6 the  $P_1(3)$  line, whereas filter 5A passes most of the entire band. Since the relative emission intensity of these spectral features depends on the temperature of the emitting region, the ratio of the column vectors  $J_1$  for any pair of the filters can be used to obtain a column vector of apparent rotational temperature.

Over the expected range of temperatures the variation of the  $P_1(3)$  line is similar to that of the entire band, so that useful rotational temperatures cannot be derived from the filter pair 6/5A. Of the other two pairs (4/5A and 4/6) the ratio from the filters 4/5A has greater precision due to the larger signal level expected from filter 5A and therefore is expected to provide more precise rotational temperatures. Although the ratio from filter pair 6/5A is relatively insensitive to temperature, it can be used to verify the precision of the temperature measurements.

The determination of rotational temperature using filter 5A is complicated by the fact that the overall filter transmission has a small but significant dependence on rotational temperature. This variation is the result of the temperature dependence of the relative intensities of the lines transmitted by the filter, combined with the nonuniform transmission curve of the filter. The effect of this variation is eliminated by the application of a correction that is applied to the observed ratios.

Unlike other WINDII measurements, hydroxyl rotational temperature is found from the ratio of the column vectors  $J_1$  for two different filters. Uncertainty in the transmission of these filters is reflected directly as a systematic error in the derived temperature. The preflight calibration of the filter transmission had an uncertainty of 5% implying a temperature uncertainty of 10 to 15 K. This uncertainty will be reduced by ground truthing. The possibility of secular changes in filter transmission means that ground truthing of rotational temperature will be required throughout the mission.

3.1.3. *Inversion of apparent quantities.* The apparent quantity column vectors  $J_1$ ,  $J_2$ , and  $J_3$ , for each of two fields



The random error standard deviation estimates calculated for the unconstrained case (i.e., all weighting factors set to 0) are the quality parameters provided with the inversion solutions. These standard deviation estimates could be considered conjunctively with the weighting factors and the choice of constraint matrices for a more thorough assessment of the quality of the atmospheric parameters. Standard deviation estimates for the retrieved solutions of flight data are provided in section 4.2.

**3.1.4. Software organization.** The scientific data production processing software (SDPPS) was developed to meet the scientific data analysis objectives of WINDII. The software is provided to NASA for use in the UARS Central Data Handling Facility (CDHF) to process scientific data from WINDII and make it available to the WINDII science team and other UARS authorized investigators. The software was supplied by the French Centre National d'Etudes Spatiales (CNES) under a memorandum of agreement between CNES and the Canadian Space Agency (CSA). It was developed under control of CNES by a French company called Dataid Eurosoft Sud Ouest, located at Toulouse, Haute Garonne, France. In accordance with NASA requirements the software architecture comprises the three following transformations. The first one reads science telemetry data called level 0 and transforms them to calibrated data called level 1. During this transformation, data are first corrected for instrument effects such as dark current subtraction and then for observatory effects such as roll effect, pixel location, and background subtraction; then they are converted to Rayleigh units. The second transformation reads calibrated data at level 1 and produces level 2 data which are vertical profiles of emission rate, temperature, and horizontal wind for both fields of view. Those deconvolved profiles from the two fields of view from the same region are then combined to obtain meridional and zonal wind profiles. The third transformation provides those temperature and wind profiles at locations specified by the UARS grid (time and latitude) called level 3A. Each transformation is split into several steps performed by an executable program, in order to insure that each step handles a smaller amount of data and provides intermediate files which give a lot of checkpoints. In addition, each elementary algorithm is performed by a specific subroutine with well-known input and output parameters which allowed easy testing during the development and facilitates the change of an algorithm to improve it. At each level and even for intermediate files, data are grouped in separate files in accordance with their type and processing level. The development of the operational version of the software spanned about 3 years, using algorithms prepared by the science team.

## 4. ERRORS AND ACCURACY

### 4.1. WINDII Characterization

For the analysis of WINDII data the instrument characteristics must be known. These include responsivity, filter bandwidth, filter transmittance, Michelson visibility, Michelson zero-wind phase, and other parameters. These quantities must be known at each wavelength at which WINDII observes and must be known as a function of position on the CCD camera. The basic characterization data are recorded as images using  $1 \times 5$  pixel bins. For atmospheric measure-

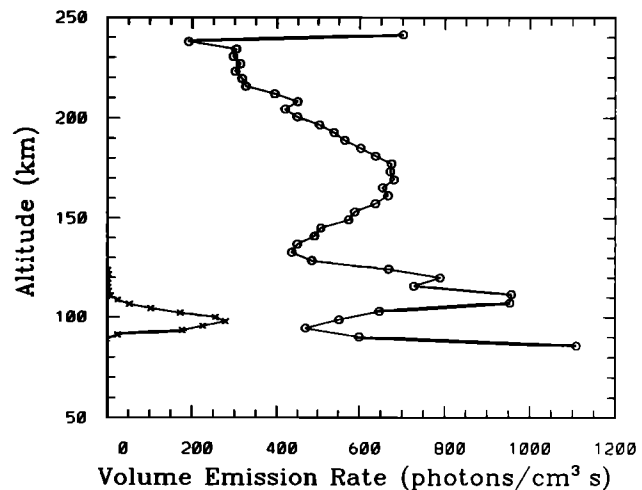


Fig. 9. Green line daytime (circles) and nighttime (crosses) volume emission rate profiles derived from the unconstrained inversion of WINDII data for field of view 1. The corresponding measurement times are 1855:56 UT on October 2, 1991, and 0554:08 UT on December 17, 1991. The reference locations for the profiles are  $8^{\circ}\text{N}$  and  $147^{\circ}\text{W}$  and  $38^{\circ}\text{S}$  and  $75^{\circ}\text{W}$ . The bins are 25 pixels wide by 4 pixels high for the daytime and 25 pixels wide by 2 pixels high for the nighttime; the sequences consist of four and eight images, respectively. The exposure in both instances is 1.024 s.

ments the bin sizes are multiples of this, so that characterization bins can be combined to determine the characterization of any other bin used in orbit. These images are stored in the CDB that is drawn upon by the SDPPS. Some aspects of this have been discussed in section 2.2.6 on the calibration package, and examples of characterization data have been shown in Plates 1, 2, 3, and 4.

### 4.2. Error Analysis Based on First Results

The results of one nighttime and one daytime set of processed green line images are presented for the purpose of assessing the potential of WINDII data, of showing the differences and similarities between day and night profiles, including the variability of the range of altitude coverage for the wind and temperature, as well as a preliminary quantitative error analysis and the impact of the linear constrained inverse model. The processing of these images for field of view one has provided the volume emission rate, Doppler wind, and temperature profiles shown in Figures 9–11. Much of the discussion in this section revolves around these figures.

The column vectors  $\mathbf{J}_1$ ,  $\mathbf{J}_2$ , and  $\mathbf{J}_3$  have been derived using the process described in section 3.1.1. with MPA. For both the night and the day cases the inversion process of section 3.1.3 is applied with all values of  $\gamma$  set to 0 (i.e., unconstrained case) and  $\gamma_E$ ,  $\gamma_{V^c}$ , and  $\gamma_{V^s}$  set to 0, 2500, and 2500, respectively, and the constraint matrix of (26).

The inverted volume emission rate profiles are superimposed in Figure 9, for two different times and locations; the narrow nighttime peak at 100 km is dramatically different from the daytime profile which extends from below 100 to about 230 km. The daytime peak at about 175 km is the “F region”, produced by the absorption of EUV radiation; the sharper peak at 110 km is produced by the recombination of atomic oxygen, the same process that produces the nighttime peak. While it is possible to impose constraints on the

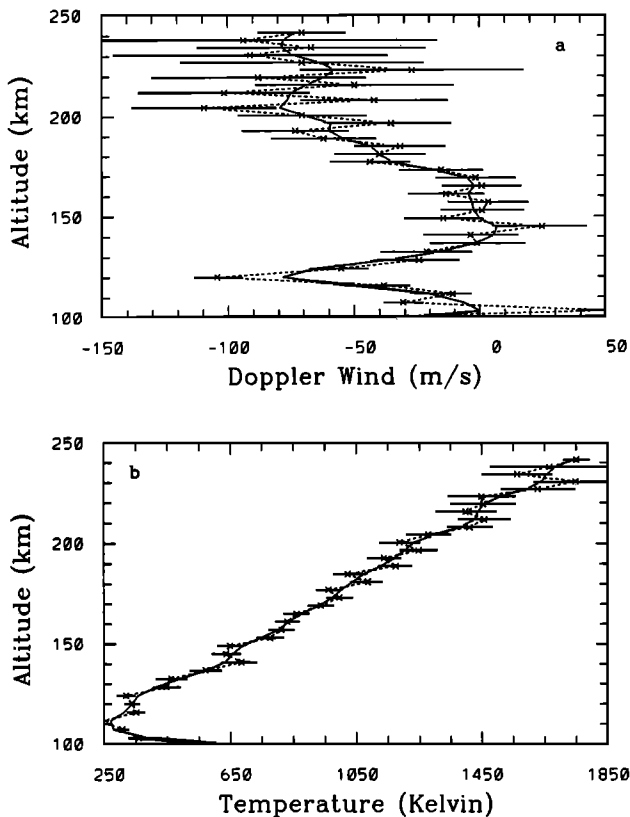


Fig. 10. (a) Doppler wind and (b) temperature profiles derived from the unconstrained (dashed) and constrained (solid) inversions of green line, daytime measurements for field of view 1. The emission line measurements consist of a sequence of four images, each with an exposure of 1.024 s, starting at 1855:56 UT on October 2, 1991. The reference location for the profiles is 8°N and 147°W. The error bars depict estimated random error standard deviations.

retrieval of volume emission rates, it seems normally not required with regard to damping noise-related oscillations. The derived standard deviation estimates for the volume emission rates of about  $1 \text{ photon cm}^{-3} \text{ s}^{-1}$  at night,  $6 \text{ photons cm}^{-3} \text{ s}^{-1}$  during the day are quite small compared to the  $280 \text{ photons cm}^{-3} \text{ s}^{-1}$  and  $960 \text{ photons cm}^{-3} \text{ s}^{-1}$  maximum volume emission rates of Figure 9. This illustrates the high signal to noise ratio required for determining winds and temperatures.

The daytime volume emission rate profile exhibits two evident features resulting from incomplete processing. The erroneously strong emission rate value near 245 km in Figure 9 is the consequence of not taking into account the significant emission contribution from above the inversion window. The addition of extra emission layers as specified in section 3.1.3 would redistribute this strong emission rate at the top end of the inversion window over a greater and more realistic altitude range. Also, the very strong feature below 100 km indicates that a more careful elimination of intense Rayleigh and/or baffle-scattered light is required; this can be achieved for future results.

The inverted wind and temperature results for the daytime profile are shown in Figures 10a, wind, and 10b, temperature. The value of 2500 for their (the last two) weighting factors is roughly equivalent to assigning wind and temperature uncertainties of 10 m/s and 30 K for the error in

complying with the profile restrictions imposed by the constraint matrix. Therefore winds and temperatures with random error standard deviation estimates much larger than these values are very likely to be strongly influenced by the constraints.

Insufficient accounting for Rayleigh and/or baffle scattering is the likely contributor to a strong temperature increase below 110 km (Figure 10b). At 110 km a temperature in the vicinity of 250 K is supported by the MSIS model. However, the temperature in the high thermosphere is several hundred degrees warmer than expected values, due to an insufficient number of collisions to thermalize the  $O(^1S)$  before radiation; the 630-nm emission will normally be used for these altitudes.

The random error standard deviation estimates shown as error bars on the figures result only from the consideration of shot noise proportional to the square root of the measured intensities, of the readout and electronic noise, and of the electron to count conversion error. Nonetheless, these are fairly well representative of the error-induced oscillations observable particularly in the profiles of Figures 10a and 10b. As demonstrated by the figures, the constraints result in the damping of such oscillations, more strongly influencing the sections of the profiles associated with larger uncer-

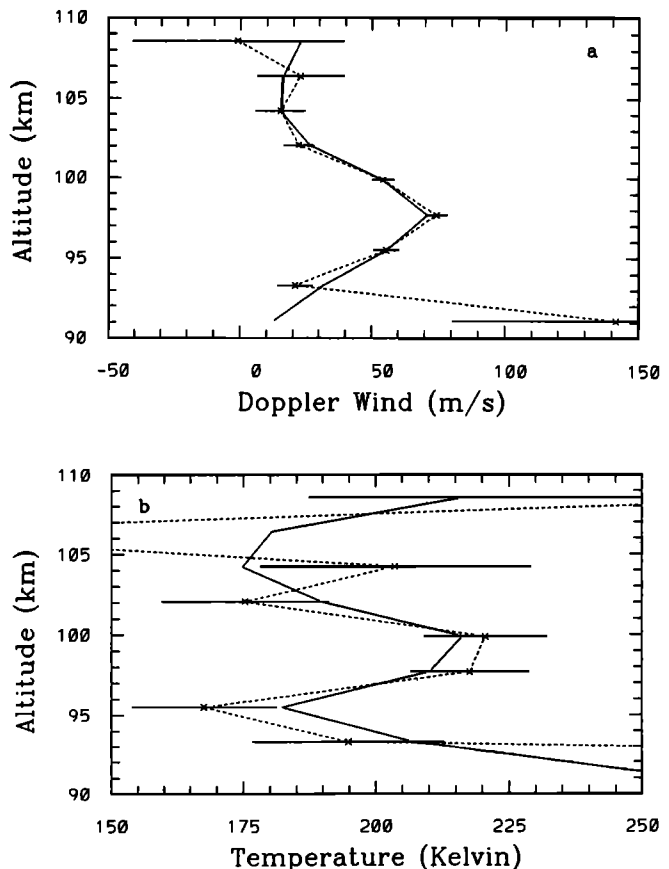


Fig. 11. (a) Doppler wind and (b) temperature profiles derived from the unconstrained (dashed) and constrained (solid) inversions of green line, nighttime measurements for field of view 1. The emission line measurements consist of a sequence of eight images, each with an exposure of 1.024 s, starting at 0554:08 UT on December 17, 1991. The reference location for the profiles is 38°S and 75°W. The error bars depict estimated random error standard deviations.

tainties. Some of the other instrumental error sources are discussed in section 2.4.

The inverted wind and temperature profiles for the nighttime measurement are shown in Figure 11a for wind and Figure 11b for temperature. For the Doppler wind and temperature the size of the standard deviation estimates is inversely related to the volume emission rates. This is illustrated by the variation in size of the errors bars in Figures 10 and 11. Consequently, for the narrow emission region of Figure 11, winds and temperatures might be considered reliable only within an altitude range of 10 to 15 km about the position of maximum emission. However, for broad emission features, such as the daytime green line emission, the usable altitude range could extend to over 100 km.

Figures 11a and 11b suggest that the linear constraints may often not significantly contribute to noise reduction particularly for the narrow 557.7-nm emission features in the high mesosphere and low thermosphere. However, the middle and high thermosphere having broader emission regions and likely smoother vertical structure may benefit more from linear constraints.

As shown in Figure 9, the volume emission rates at night can be significantly weaker and the emission region much narrower than during the day. However, since the larger instrument nighttime aperture permits more light to enter the instrument at night, the nighttime winds and temperatures about the narrow emission region may be as reliable as the daytime values. This is clearly evident when comparing the error bars of Figures 10 and 11; the minimum standard deviations for the wind and temperature are located at or near the altitudes of maximum emission and have values of 4 m/s and 11 K at night and of 7 m/s and 20 K during the day.

While the vertical profiles shown seem reasonable at first glance, these results cannot as yet be considered as final products; considerable work remains to be done before the data products are validated. Still the data shown confirm the potential high quality of the ultimate products that will be generated and that the goals established for WINDII can be achieved.

The preliminary results presented in this paper have been selected to demonstrate the wind measurement capability for WINDII, and for this purpose we have chosen the 557.7-nm OI emission because it is a relatively simple atomic emission and because it gives the greatest altitude coverage. Less attention has been given to the other emissions with respect to validation, but the data for all have been closely examined, and we briefly note our observations here.

The 630-nm OI data are very good and will provide winds and Doppler temperatures above the altitude limit of the 557.7-nm data. This emission has a lower priority than the others and is observed 1 day per week. The daytime emission is consistently strong, while the nighttime levels are more variable. However it will be possible to obtain winds from all but the very weakest nighttime data, in the early morning hours when the *F* region is most depleted.

The hydroxyl data are excellent and will provide a wealth of information on the emission rate, temperatures, and winds near the mesopause. The fringe modulation is very good, indicating that the choice of optical path difference, as discussed in section 2.2.1, was appropriate. The signal level is good, although it is the weakest of the nighttime emissions that we observe. A typical signal level for the Doppler

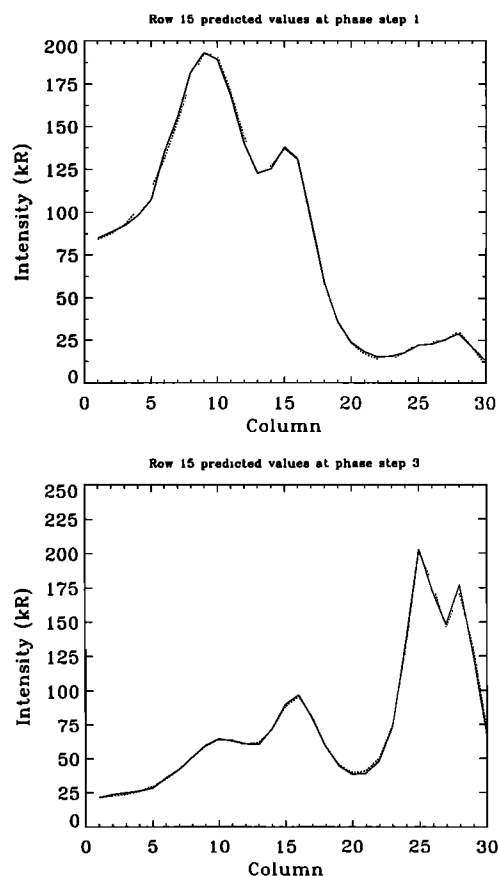


Fig. 12. (a) Apparent emission rate versus CCD column number for one full row of bins for several lines of the O<sub>2</sub> atm band (see text) observed in daytime (solid curve). This is for a single image corresponding to Michelson mirror step 1. The dashed curve is the fit to these data obtained in the analysis. (b) The same as (a) but for mirror step 3, different in phase from that in (a) by 180°. Note the large changes in signal level arising from the modulation of the interferometer.

channel (filter 6) is 1000 ADU for 2 × 25 pixel binning and 4 s exposure time.

Imaging the O<sub>2</sub> atmospheric band is the most challenging of the WINDII observations because of the closely spaced rotational lines. The approach used is to fit an entire row of data at one time. In Figure 12a the observed emission rate (solid curve) and derived fit across a row (dashed curve) in FOV 1 in an O<sub>2</sub> daytime image is shown for Michelson mirror step 1. The spatial/spectral filtering of the interference filter spreads the four O<sub>2</sub> lines being viewed (the <sup>P</sup>P(7), <sup>Q</sup>P(7), <sup>P</sup>P(5), and <sup>Q</sup>P(5) lines from right to left in each panel) across the row. In Figure 12b we show the same row and the same measurement for mirror step 3, 180° different in phase from step 1. The strong modulation of these lines demonstrated by the large change in signal levels between Figures 12a and 12b confirms the correct choice of optical path difference. The goodness of the fit is particularly noteworthy as it requires an accurate estimation of both the filter and the Michelson parameters. Because of the narrow filter passband it was not possible to assume that the passband in orbit was the same as that measured on the ground. There is sufficient spectral information to deduce the filter characteristics from the data and that is what has been done in the fitting process. The derived phases from each of

the four lines are consistent with one another, giving confidence in the wind results obtained.

The 732/733 nm  $O^+$  emission has received the least attention. This is the weakest emission observed, giving ADU levels of 1000 in the daytime for  $10 \times 25$  pixel binning and exposure times of 4 s. The modulation is good, confirming the correct choice of OPD, and so we have good expectations of determining useful ion wind data. Because of the multiple lines involved, a similar procedure will be used as for the  $O_2$  atm band.

#### 4.3. WINDII Validation

Although considerable effort was made to characterize the WINDII instrument on the ground, so that it would provide accurate data in orbit, a program has also been established to validate the values obtained in orbit, under flight conditions. The overall approach makes use of three levels of comparison measurement: (1) those using a similar type of Michelson interferometer on the ground; (2) those using the same method, namely, the optical Doppler airglow measurement but with a Fabry-Perot spectrometer rather than a Michelson interferometer; and (3) those using a completely different method such as a radar, or a chemical trail released from a rocket.

An extensive validation program is being conducted with the French MICADO instrument at the Observatoire d'Haute Provence, an instrument that has already established a successful program of wind and temperature measurements. A new Canadian instrument called GWAMDI has been assembled at York University around the original WAMDI Michelson interferometer and is being operated at Bear Lake, Utah. This site was chosen because at  $42^\circ$  latitude it is at the turning point of WINDII's fields of view, as the satellite turns around at  $57^\circ$ . This ensures at least one overpass per night. A second similar instrument but with the capability of measuring winds from the  $O_2$  atm (0,1) band is being brought into operation. The NASA correlative measurements program is supporting V. Wickwar and T. L. Killeen in operating their Fabry-Perot instruments in conjunction with WINDII overflights. The problem in comparing optical measurements made in space with those made on the ground is that the integrating paths through the emission layer are different. Since WINDII data are inverted to vertical profiles, it is possible to use these data to simulate the results of integrating along the path seen from the ground; it is these simulations that will be compared with the ground-based observations. Where the emitting atmosphere is horizontally homogeneous, the results are expected to agree; but in the presence of gradients or wave structures, they may not. In order to assess this, ground-based imagers of the emissions observed by WINDII will be employed at the validation sites. The one correlative instrument that does not have this problem is HRDI; it can make simultaneous measurements along the same integrating path as WINDII, and these intercomparisons will be particularly useful. But nevertheless, it is important that measurements be made by completely independent methods. The NASA correlative measurements program also sponsors the radar measurements of D. Fritts and C. Gardner in support of WINDII. WINDII coinvestigators are also organizing correlative measurements with the EISCAT, Millstone Hill, and Arecibo incoherent scatter radars.

As well as winds and Doppler temperatures it is important that the rotational temperature measurements from OH and  $O_2$  be validated as well. UWOMI, an IR Fourier transform spectrometer (FTS) constructed at the University of Western Ontario is being operated at Fort Collins for the validation of OH rotational temperatures; a similar instrument will be operated at Observatoire d'Haute Provence. Another FTS is being operated by P. Espy (supported by NASA) at Bear Lake, and as well there is a spectral imager for rotational temperature measurement of OH by G. Swenson (supported by NASA), and York University is operating its MORTI instrument [Wiens *et al.*, 1991] for the rotational temperature measurements of the  $O_2$  atm band. Together with other measurements worldwide not mentioned here, there is thus a very extensive body of ground-based measurements being assembled for the validation of WINDII.

## 5. OPERATING MODES AND OBSERVING STRATEGY

### 5.1. Observation Mode

For a given measurement the WINDII operator must make an appropriate selection of interference filter, camera exposure time, and CCD window and bin sizes. In order to provide flexibility in combining these various instrumental parameters while at the same time limiting the number of possibilities to include only combinations which are useful, a scheme of filter groups was devised from which orbit by orbit observing scenarios are developed. A filter group defines the exposure time and bin and window dimensions to be used with any one of the seven interference filters. Filter groups are used in certain combinations called cycles, and these combinations are set by the cycle definition table. Cycles are then chosen from the list to compile orbit sequences, two of which can be stored at one time.

The current list of filter group definitions is given in Table 7. The mnemonic is the identifier of the group used by the command planning computer to generate daily activity plans that are eventually uploaded to UARS. The number of images in a measurement sequence is shown in column 3; for a background measurement only one is required, but for a Doppler measurement, eight images are normally taken (in steps of  $45^\circ$ ); but an alternative is a sequence of four (in steps of  $90^\circ$ ), repeated again (4R). The column labelled "Bins" gives the number of pixels in a bin. The first number ( $V$ ) gives a measure of the vertical resolution, remembering that one pixel corresponds to about 1 km at the limb (it varies with altitude). Column 5 gives the tangent altitude of the bottom of the window, and column 6, when added to column 5, gives the tangent altitude of the top of the window. The window size is intended to include only those bins that receive light from the layer being observed in order to reduce the transmission time. Because the Earth is oblate rather than spherical, and the UARS orbit is slightly elliptical, the window position has to change with orbit angle. Such a change is triggered by an "oblateness" signal from UARS whenever the tangent point altitude of the boresight changes by 2.5 km.

Filter groups are combined into filter cycles according to Table 8, and the current list of orbital sequences is given in Table 9. Usually a single orbital sequence is used for a full 24-hour day of universal time, so the orbit must include at least one day cycle and one night cycle. The red day filter

TABLE 7. WINDII Filter Group Specifications

Common Name	Mnemonic*	No. of Images	Bins $V \times H$	Altitude, km	Range, km	Exposure Time, s
Red day background	DF3B1	1	8 × 25	84	230	1.02
Red day	DF3R	4R	8 × 25	92	225	1.02
O <sub>2</sub> day	DF7E	8	2 × 10	75	40	2.05
O <sub>2</sub> day 3 × 10	DF7E <sub>3</sub>	8	3 × 10	65	60	2.05
Green day mesosphere bkg.	DMF2B1	1	2 × 25	71	48	1.02
Green day mesosphere	DMF2E	8	2 × 25	75	40	1.02
Green day thermosphere background	DTF2B1	1	4 × 25	101	215	1.02
Green day thermosphere	DTF2E	8	4 × 25	105	215	1.02
O <sup>+</sup> day background	DTF4B6	1	12 × 25	88	230	3.97
O <sup>+</sup> day	DTF4R	4R	12 × 25	92	225	3.97
Red night background	NF3B1	1	6 × 25	105	215	1.54
Red night	NF3R	4R	6 × 25	110	205	1.54
O <sub>2</sub> night	NF7E	8	2 × 10	75	45	2.05
Green night mesosphere background	NMF2B1	1	2 × 25	70	48	2.05
Green night mesosphere	NMF2E	8	2 × 25	74	40	2.05
OH background	NMF4B5	1	2 × 25	70	61	3.97
OH rotational temperature	NMF4F	4	2 × 25	70	61	3.97
OH whole band	NMF5F	4	2 × 25	70	61	3.97
OH wind	NMF6E	8	2 × 25	70	61	3.97
Green night thermosphere background	NTF2B1	1	4 × 25	100	215	2.05
Green night thermosphere	NTF2E	8	4 × 25	104	215	2.05

\*D, day; N, night; F, measurement filter (filter number follows); B, background filter (filter number follows); M, mesosphere; T, thermosphere; F (terminal), four; E, eight; R, repeated.

cycle requires eight images taken with filter 3 (630 nm) and one with the same exposure time, window, and binning through the background filter 1. The red night cycle is nearly the same, but the aperture must be set for night and the window and bin sizes are slightly reduced. Filter cycles designed around the green line (558 nm, filter 2) are complicated by the existence of two layers, one in the lower and one in the middle thermosphere, both of which have very different temperature and wind characteristics. Two sets of measurements (*M* and *T*) are made with different overlapping windows and different bins and then combined in the data processing into a single large image. The O<sub>2</sub> filter cycles are the simplest because the background is derived between the rotational lines, without a separate filter.

Because the timing of the cycles within the orbital sequences is important, elaborate command planning software has been developed to assist the operator in this task. In the interest of gathering a geographically dense data set the filter

cycles should waste as little time as possible. The total time allotted to one cycle is listed in Table 8, and the distance moved by the tangent point during that time at 7 km/s is also shown. This time includes the sum of all the exposure times, the time to move the filter wheel, and the time to transfer the image via the telemetry system. Cycles must be spaced so that the volume of atmosphere measured by the afterward field of view is the same one measured in some earlier cycle by the forward field of view. This progression must be carefully broken into by a frequent calibration cycle at least once every 15 min to monitor the dark count and phase of WINDII. Furthermore, the orbital sequence has to begin when both fields of view are on the same side of the solar terminator. Additional constraints are imposed during correlative measurement periods with ground observatories in that calibrations should not take place during the time when either WINDII field of view overlaps the field of view of the ground-based instrumentation. An interactive plotting pro-

TABLE 8. WINDII Filter Cycle Definitions

Common Name	Mnemonic Sequence	Period, s	Distance, km
Green day	DTF2B1 DTF2E DMF2B1 DMF2E	65.0	443
Green night	NTF2B1 NTF2E NMF2B1 NMF2E	68.6	467
Red day	DF3B1 DF3R	23.0	162
Red night	NF3B1 NF3R	28.7	203
O <sup>+</sup> day	DTF4B6 DTF4R	45.1	318
OH night	NMF5F NMF4F NMF6E	86.0	586
O <sub>2</sub> day	DF7E <sub>3</sub>	40.7	277
O <sub>2</sub> night	NF7E	53.2	362
Green/red day	DTF2B1 DTF2E DF3B1 DF3R		
Green/red night	NMF2B1 NMF2E NF3B1 NF3R		
Green/OH	NMF2B1 NMF2E NMF5F NMF6E		
OH/O <sub>2</sub> night	NMF5F NMF6E NF7E		
OH short	NMF4B5 NMF4F NMF6E		
O <sub>2</sub> /green day	DF7E DMF2B1 DMF2E		
O <sub>2</sub> /green night	NF7E NMF2B1 NMF2E		

Blank in columns 3 and 4 means that the cycle has never been used.

TABLE 9. WINDII Orbital Sequence Options

Common Name	Cycle Composition	Measurements	Vertical, Day	Extent, km, Night
Green	Green day, green night	W, Dt	75-320	85-110
O <sub>2</sub>	O <sub>2</sub> day, O <sub>2</sub> night	W, RT	75-120	85-105
O <sup>+</sup> /OH	O <sup>+</sup> day	ID	92-320	
	OH night	W, RT		75-100
Red	Red day, red night	W, DT	92-320	110-320
Green/O <sub>2</sub>	O <sub>2</sub> /green, day and night	W,RT,DT	75-320	75-105
Green/OH	Green day, green/OH night	W,RT,DT	85-320	75-110
Mesopause	O <sub>2</sub> /green day, OH/O <sub>2</sub> night	W,RT,DT	75-320	75-105
Red	Red day, red night	W, DT	92-320	110-320
Green/O <sub>2</sub>	O <sub>2</sub> /green, day and night	W,RT,DT	75-320	75-105
Green/OH	Green day, green/OH night	W,RT,DT	85-320	75-110
Mesopause	O <sub>2</sub> /green day, OH/O <sub>2</sub> night	W,RT,DT	75-320	75-105

W, Doppler wind; DT, Doppler temperature; ID, ion drift; RT, rotational temperature.

gram computes all of these times when given the starting place and time of the orbital sequence by the operator, who may then change and restart as needed. The operator-approved time line is automatically written into a microprocessor programming change which is loaded through an upward telemetry link once per day. Scientifically, the primary goal of WINDII is to provide global coverage of winds and temperatures and that global coverage is most continuous if a single wavelength, or wavelength pair, is observed continuously for a full 1 or 2 days. A weekly rota has therefore been established that consists of green, O<sub>2</sub>, O<sup>+</sup> (or green)/OH, green, O<sub>2</sub>, O<sup>+</sup> (or green)/OH, and red for Sunday through Saturday. The rota offers a balance between upper and lower thermospheric measurements that is consistent with the UARS mission, and the weekly period makes it easily compatible with the personnel work week. Changes to this basic plan are frequent and usually triggered by the schedules of ground-based correlative measurement investigators. In any case, a daily science plan is always prepared at least 4 days in advance in a format similar to the example of an O<sup>+</sup>/OH day in Table 10.

### 5.2. Nonobservation Modes

During WINDII's normal observation modes a frequent calibration is made approximately every quarter hour to monitor the dark count and any phase drifts detectable using one of the four spectral calibration lamps. A more complete calibration, called the infrequent calibration, is performed only once per week because it requires a full orbit of time

and because it employs two limited lifetime components, the tungsten ribbon broadband source and the laser. In this mode the calibration mirrors are deployed, phase measurements are made with all four spectral lamps, and the dark count is measured. Images are taken using the tungsten source with all filters to calibrate responsivity, and a series of measurements is made with the laser to calibrate the WINDII visibility. Results of these calibrations are stored and compared with previous values in the CDB. A second nonobservation mode is the star map mode, in which the calibration mirrors are retracted and the filter wheel is rotated to the eighth or blank position. In this configuration, single images with 1 × 1 binning are made, from which the look directions of both fields of view can be measured relative to the known star fields to monitor the attitude of UARS. The safhold mode is one which deploys the calibration mirrors to exclude outside light and removes the power from the CCD camera, its associated electronics, and all calibration lamps. This mode is used during UARS yaw-around operations or other situations in which the safety of the instrument may be in question. It differs from the "OFF" state in that the temperature stabilization system remains operative for quick return to observation mode.

The line of sight of each of the two WINDII fields of view can be determined to a good approximation by relating the instrument reference frame to the spacecraft reference frame followed by a transformation based on information obtained from the UARS Orbit and Attitude Services. To maximize the scientific value of the WINDII data in the mesopause region, the peak altitudes of the narrow emission layers must be determined with an absolute accuracy of about 1 km at the limb. This requires that the attitude information be carefully verified and occasionally monitored. For this reason the WINDII operations plan includes high-resolution imaging of numerous star fields under various operating conditions. By careful selection of stars in the field and by appropriate centroiding, the attitude can be determined sufficiently accurately. This information can then be fed back through the various reference frames to provide a correction matrix to be used in the analysis of the WINDII images. In addition, this auxiliary attitude information could prove to be a valuable tool in the analysis of other attitude sensitive data.

TABLE 10. Daily Science Plan Example, O<sup>+</sup>/OH

WINDII
Hemisphere of perigee, north
View from orbit plane, north
Mnemonics
DTF4B6, DTF4R
day, background, O <sup>+</sup>
NMF5F, NMF4F, NMF6E
night, OH band, rotational temperature, wind
Purpose, day, oxygen ion (O <sup>+</sup> , 90-315 km and 12 km vertical resolution
Night, hydroxyl molecule (OH), 70-130 km and 2 km vertical resolution
Products, winds, temperature, emission rates

## 6. DISCUSSION AND CONCLUSIONS

The WINDII science team placed requirements on WINDII that would allow it to measure winds and temperatures from about 80 to 300 km, using the OH, O<sub>2</sub> atm, O(<sup>1</sup>S), O(<sup>1</sup>D), and O<sup>+</sup>(<sup>2</sup>P) emissions. When this was done, in 1985, one could not be sure that these requirements would be met. However, with careful attention to the incorporation of excellent surface flatness and thermal stability of the Michelson interferometer, high system transmission, and low CCD noise level, the requirements have all been met or exceeded. The Michelson interferometer does not absorb light, it only modulates it. The imaging system, despite a large number of surfaces, has a transmittance of about 75%, and the interference filters have transmittances of up to 80%. The bare CCD has a quantum efficiency of about 60%, so that, overall, WINDII is approaching the ultimate limit for system responsivity, with a spectral resolution capable of distinguishing wavelength shifts as small as  $2 \times 10^{-5}$  nm, or 20 fm. The ability to form windows and bins on the CCD gives the instrument its flexibility and power to deal with a wide range of signal and calibration requirements; it has made a very complex instrument possible to use in an effective way. In addition, we have an enormously greater understanding of the instrument owing to the imaging aspect of the characterization. The single-stage baffle, with its knife edge and the technique of inserting a daytime aperture, worked extremely well and since the launch on September 12, 1991, has permitted excellent measurements of the atomic oxygen 557.7-nm emission in the daytime.

*Acknowledgments.* The WINDII project was jointly sponsored by the Canadian Space Agency and the Centre National d'Etudes Spatiales. The authors are grateful for their dedicated commitment and loyal support. They are indebted to the prime contractor, AIT Corporation and the principal subcontractor responsible for the design and fabrication of the flight instrument, CAL Corporation. While all the industries with a major involvement are represented by the coauthors, there are a very large number of individuals in those organizations whose names do not appear. One of these is T. Darlington, the CSA project manager throughout much of the project. We owe a particular debt of gratitude to all those whose names do not appear but made essential contributions to this project. The work done by SED Systems on the WAMDII instrument laid the foundations for the basic approach and proved the concept upon which WINDII was based. Support for the participation of scientists during the development phase, but particularly during the science analysis phase, is provided by the Centre National de la Recherche Scientifique (CNRS) and by the Natural Sciences and Engineering Research Council of Canada. The Institute for Space and Terrestrial Science, a designated Centre of Excellence supported by the Technology Fund of the Province of Ontario, has also contributed to the development of algorithms, to the instrument validation, and will contribute to the science analysis. Individual organizations have supported their own coauthors in various ways. Two organizations which are not represented here but provided consistent encouragement and constant support are NASA and General Electric; the WINDII team is grateful for their help in making this project a success.

## REFERENCES

- Andrews, D. G., J. R. Holton, and C. B. Leovy, *Middle Atmosphere Dynamics*, Academic, San Diego, Calif., 1987.
- Batten, S., and D. Rees, Thermospheric winds in the auroral oval: Observations of small scale structures and rapid fluctuations by a Doppler imaging system, *Planet. Space Sci.*, **38**, 675, 1990.
- Bevington, P. R., *Data Reduction and Error Analysis for the Physical Sciences*, McGraw-Hill, New York, 1969.
- Blamont, J., and J. M. Luton, Geomagnetic effect on the neutral temperature of the F region during the magnetic storm of September 1969, *J. Geophys. Res.*, **77**, 3534, 1972.
- Bouchareine, P., and P. Connes, Interferometer with compensated field for Fourier transform spectroscopy, *J. Phys.*, **24**, 2, 134, 1963.
- Burnside, R. G., F. A. Herrero, J. W. Meriwether, and J. C. G. Walker, Optical observations of thermospheric dynamics at Arecibo, *J. Geophys. Res.*, **86**, 5532, 1981.
- Dobrowolski, J. A., F. C. Ho, and A. Waldorf, Beam splitter for a wide-angle Michelson Doppler imaging interferometer, *Appl. Opt.*, **24**, 1585, 1985.
- Evans, W. F. J., I. C. McDade, J. Yuen, and E. J. Llewellyn, A rocket measurement of the O<sub>2</sub> infrared atmospheric (0-0) band emission in the dayglow and a determination of the mesospheric ozone and atomic oxygen densities, *Can. J. Phys.*, **66**, 941, 1988.
- Forbes, J. M., Atmospheric tides, 1, Model description and results for the solar diurnal component, *J. Geophys. Res.*, **87**, 5222, 1982a.
- Forbes, J. M., Atmospheric tides, 2, The solar and lunar semidiurnal components, *J. Geophys. Res.*, **87**, 5241, 1982b.
- Hays, P. B., T. L. Killeen, N. W. Spencer, L. E. Wharton, R. G. Roble, B. A. Emery, T. J. Fuller Rowell, D. Rees, L. A. Frank, and J. D. Craven, Observations of the dynamics of the polar thermosphere, *J. Geophys. Res.*, **89**, 5165, 1984.
- Hedin, A. E., MSIS 86 thermospheric model, *J. Geophys. Res.*, **92**, 4649, 1987.
- Hernandez, G., R. G. Roble, E. C. Ridley, and J. H. Allen, Thermospheric response observed over Fritz Peak, Colorado, during two large geomagnetic storms near solar cycle maximum, *J. Geophys. Res.*, **87**, 9181, 1982.
- Hilliard, R. L., and G. G. Shepherd, Wide-angle Michelson interferometer for measuring Doppler line widths, *J. Opt. Soc. Am.*, **56**, 362, 1966a.
- Hilliard R. L., and G. G. Shepherd, Upper atmospheric temperatures from Doppler line widths, *Planet. Space Sci.*, **14**, 383, 1966b.
- Kendall, D. J. W., et al., OGLow—An experiment to measure orbit and earth optical emissions, *Can. Aeronaut. Space J.*, **31**, 227, 1985.
- Killeen, T. L., and R. G. Roble, Thermosphere dynamics: Contributions from the first 5 years of the Dynamics Explorer program, *Rev. Geophys.*, **26**, 329, 1988.
- Killeen, T. L., P. B. Hays, G. R. Carignan, R. A. Heelis, W. B. Hanson, N. W. Spencer, and L. H. Brace, Ion-neutral coupling in the high-latitude F region: Evaluation of ion heating terms from Dynamics Explorer 2, *J. Geophys. Res.*, **89**, 7495, 1984.
- Llewellyn, E. J., and I. C. McDade, Singlet molecular oxygen in planetary atmospheres, *J. Photochem.*, **25**, 379, 1984.
- Marks, C. J., Some features of the middle atmosphere revealed by Nimbus 5 and 6, *J. Atmos. Sci.*, **46**, 2485, 1989.
- McDade, I. C., D. P. Murtagh, R. G. H. Greer, P. H. G. Dickinson, G. Witt, J. Stegman, E. J. Llewellyn, L. Thomas, and D. B. Jenkins, ETON 2: Quenching parameters for proposed precursors of O<sub>2</sub>(b<sup>1</sup>Σ<sup>+</sup>) and O(<sup>1</sup>S) in the terrestrial nightglow, *Planet. Space Sci.*, **34**, 789, 1986.
- McDade, I. C., W. E. Sharp, P. G. Richards, and D. G. Torr, On the inversion of O<sup>+</sup> 2P – 2D) 7320 Å twilight airglow observations: A method for recovering both the ionization frequency and the thermospheric oxygen atom densities, *J. Geophys. Res.*, **96**, 259, 1991.
- Mende, S. B., G. R. Swenson, E. J. Llewellyn, W. Denig, D. J. W. Kendall, and T. G. Slanger, Measurements of rotational temperature in the airglow with a photometric imaging etalon spectrometer, *J. Geophys. Res.*, **93**, 12,861, 1988.
- Murtagh, D. P., J. Stegman, G. Witt, E. J. Llewellyn, and I. C. McDade, A twilight measurement of the OH(8-3) Meinel band and atmospheric temperature, *Planet. Space Sci.*, **35**, 1149, 1987.
- Powell, I., Optical system design for the WAMDII instrument, *J. Soc. Photoopt. Instrum. Eng.*, **655**, 198, 1986.
- Randel, W. J., The Evaluation of winds from geopotential height data in the stratosphere, *J. Atmos. Sci.*, **44**, 3097, 1987.
- Rees, D., A. H. Greenaway, R. Gordon, I. McWhirter, P. J. Charleton, and Å. Steen, The Doppler Imaging System, Initial observations of the auroral thermosphere, *Planet. Space Sci.*, **32**, 273, 1984.

- Richmond, A. D., The neutral atmosphere, in *Geomagnetism*, vol. 4, edited by J. A. Jacobs, Academic, San Diego, Calif., 1991.
- Rodgers, C. D., Retrieval of atmospheric temperature and composition from remote measurements of thermal radiation, *Rev. Geophys.*, *14*, 609, 1976.
- Shepherd, G. G., et al., Optical Doppler imaging of the aurora borealis, *Geophys. Res. Lett.*, *11*, 1003, 1984.
- Shepherd, G. G., et al., WAMDII: Wide-angle Michelson Doppler imaging interferometer for Spacelab, *Appl. Opt.*, *24*, 1571, 1985.
- Shepherd, G. G., W. A. Gault, and R. A. Koehler, The development of wide angle Michelson interferometers in Canada, *Can. J. Phys.*, *69*, 1175, 1991.
- Shine, K. P., Sources and sinks of zonal momentum in the middle atmosphere diagnosed using the diabatic circulation, *Q. J. R. Meteorol. Soc.*, *115*, 265, 1989.
- Solomon, S., J. T. Kiehl, R. R. Garcia, and W. Grose, Tracer transport of the diabatic circulation deduced from satellite observations, *J. Atmos. Sci.*, *43*, 1603, 1986.
- Swenson, G. R., S. B. Mende, and K. S. Clifton, Ram vehicle glow spectrum; Implication of NO recombination continuum, *Geophys. Res. Lett.*, *12*, 97, 1985.
- Swenson, G. R., S. B. Mende, and E. J. Llewellyn, Imaging observations of lower thermospheric ( $O^1S$ ) and  $O_2$  Airglow emissions from STS 9: Implications of height variations, *J. Geophys. Res.*, *94*, 1417, 1989.
- Thuillier, G., and M. Hersé, Thermally stable field compensated Michelson interferometer for measurement of temperature and wind of the planetary atmospheres, *Appl. Opt.*, *30*, 1210, 1991.
- Thuillier, G., and G. G. Shepherd, Fully compensated Michelson interferometer of fixed path difference, *Appl. Opt.*, *24*, 1599, 1985.
- Thuillier, G., J. L. Falin, and F. Barlier, Geomagnetic activity effect on the exospheric temperatures at high latitudes, *J. Atmos. Terr. Phys.*, *42*, 653, 1980.
- Thuillier, G., C. Lathuillère, M. Hersé, C. Senior, W. Kofman, M.-L. Duboin, D. Alcaydé, F. Barlier, and J. Fontanari, Coordinated EISCAT-MICADO interferometer measurements of neutral winds and temperatures in E- and F-regions, *J. Atmos. Terr. Phys.*, *52*, 625, 1990.
- Thuillier, G., J. F. Brun, J. M. Alunni, and J. J. Roland, Frequency stabilized He-Ne laser for the WINDII interferometer calibration on board the UARS satellite, *Opt. Eng.*, in press, 1992.
- Title, A. M., and H. E. Ramsey, Improvements in birefringent filters, 6, Analog birefringent elements, *Appl. Opt.*, *19*, 2046, 1980.
- Twomey, S., On the numerical solution of Fredholm integral equations of the first kind by the inversion of the linear systems produced by quadrature, *J. Assoc. Comput. Mach.*, *10*, 97, 1963.
- Twomey, S., *Introduction to the Mathematics of Inversion in Remote Sensing and Indirect Measurements*, Development in Geomathematics series, Elsevier, New York, 1977.
- U.S. Government Printing Office, U.S. Standard Atmosphere, 1976, *NOAA-S/T 76-1562*, Washington, D. C., 1976.
- Ward, W. E., The design and implementation of a wide-angle Michelson interferometer to observe thermospheric winds, Ph.D. thesis, 373 pp., York Univ., Toronto, 1988.
- Ward, W. E., Z. Pasturczyk, W. A. Gault, and G. G. Shepherd, Multiple reflections in a wide-angle Michelson interferometer, *Appl. Opt.*, *24*, 1589, 1985.
- Wiens, R. H., G. G. Shepherd, W. A. Gault, and P. R. Kosteniuk, Optical measurements of winds in the lower thermosphere, *J. Geophys. Res.*, *93*, 5973, 1988.
- Wiens, R. H., S.-P. Zhang, R. N. Peterson, and G. G. Shepherd, MORTI: A mesopause oxygen rotational temperature imager, *Planet. Space Sci.*, *39*, 1363, 1991.
- J. M. Alunni, Quantel, B.P. 23, 91941 Les Ulis - Orsay, France.
- S. Brune, D. Harvie, and J. Ohrt, AIT Corporation, 9 Auriga Drive, Ottawa, Canada, K2E 7T9.
- P. Charlot and F. Girod, CNES Centre Spatial de Toulouse, Toulouse, France.
- L. L. Cogger, Department of Physics, University of Calgary, Calgary, Alberta, Canada, T2N 1N4.
- D.-L. Desaulniers, CAL Corporation, 1050 Morrison Drive, Ottawa, Ontario, Canada, K2H 8K7.
- W. F. J. Evans, Trent University, Peterborough, Ontario, Canada, K9J 7B8.
- R. H. Hum and D. J. W. Kendall, Canadian Space Agency, P. O. Box 7275, Vanier Postal Station, Ottawa, Ontario, Canada, K1L 8E3.
- E. J. Llewellyn, Institute for Space and Atmospheric Science, University of Saskatchewan, Saskatoon, Saskatchewan, Canada S7N 0W0.
- R. P. Lowe, Department of Physics, University of Western Ontario, London, Ontario, Canada, N6A 3K7.
- F. Pasternak, MATRA-ESPACE, 31055, Toulouse, France.
- O. Peillet, SOCIETE BERTIN and Cie, B.P. 22, Z.I. 13762, Aix les Milles, France.
- G. G. Shepherd, W. A. Gault, B. H. Solheim, C. Hersom, Y. Rochon, W. E. Ward, and R. H. Wiens, Institute for Space and Terrestrial Sciences, York University, North York, Ontario, Canada, M3J 1P3.
- G. Thuillier and J.-F. Brun, Service D'Aéronomie du CNRS, Verrières-le-Buisson, France.

(Received February 18, 1992;  
revised January 21, 1993;  
accepted January 21, 1993.)